Waves explain observed similarity scaling of turbulence dissipation in the Southern Ocean

Isabelle Giddy[a,b,g] , Daniel Whitt[b] , Ilker Fer[c] , Sebastiaan Swart[a,d] , Øyvind Breivik[c,e] , Sarah-Anne Nicholson[f]

[a] *University of Gothenburg, Sweden*

[b] *NASA Ames Research Center, California, USA*

[c] *Geophysical Institute, University of Bergen, Norway*

[d] *Department of Oceanography, University of Cape Town, Rondebosch, South Africa*

[e] *Norwegian Meteorological Institute, Norway*

[f] *Southern Ocean Carbon-Climate Observatory, Smart Places, CSIR, South Africa*

[g] *California State University Montery Bay, USA*

Corresponding author: Isabelle Giddy, isabelle.giddy@gu.se

ABSTRACT: We investigate the turbulence kinetic energy (TKE) budget of the upper ocean and its response to wind and wave forcing in the Southern Ocean, using realistically forced Large Eddy Simulations (LES) and in situ microstructure shear observations. The widely used law-of-the-wall similarity scaling assumes that shear production of TKE is balanced by its dissipation. However, our findings reiterate that this assumption is violated under wave forcing: dissipation is primarily balanced by local Stokes shear production, augmented by almost equal contributions from local Eulerian shear production and non-local convergence of TKE transport. Despite this, the canonical law-of-the-wall scaling reasonably describes the vertical distribution of dissipation rates in the boundary layer in both realistically-forced LES and observations, even though the underlying physical reasoning does not hold. We propose a modified scaling to account for the non-local component of the TKE budget that yields accurate predictions of the TKE budget as well as an interpretation accounting for wave effects. These insights have important implications for interpreting turbulence dissipation rate observations.

SIGNIFICANCE STATEMENT: This study provides and evaluates a physical model of turbulence in the near surface layer of the Southern Ocean under strong winds and waves. **This turbulence model quantifies how the vertical transport and dissipation of turbulence relate to the production of turbulence due to winds and waves**. This model of turbulence is valuable because the Southern Ocean plays a key role in regulating climate through the uptake of heat and carbon from the atmosphere, which is mediated by small-scale turbulent motions that generally must be estimated without turbulence observations in global ocean and climate simulations. In addition, this model provides insight into dissipation rate observations, which are generally collected without observations of the corresponding turbulence production and transport.

1. Introduction

The Southern Ocean plays a disproportionately important role in the climate system due to its capacity to absorb carbon and heat (Williams et al. 2024; Gruber et al. 2019; Marshall et al. 2015). This uptake occurs through exchanges of momentum, heat, tracers and gases in the ocean surface boundary layer (OSBL) that are regulated by small-scale turbulent motions. These turbulent motions must be parameterized in ocean models. Furthermore, because turbulence generation is concentrated in the surface layer—the uppermost 10% of the OSBL—it is essential to accurately represent the ocean surface layer's response to atmospheric and wave forcing.

Turbulence in the surface layer is often described using frameworks originally developed for the atmospheric boundary layer, where surface stress drives local shear production near a rigid boundary. However, in contrast to the atmosphere which is treated as a no-slip boundary, the ocean surface is strongly influenced by both breaking and non-breaking surface gravity waves, that modify turbulence production and transport. Breaking waves enhance dissipation in the near-surface layer ($\sim$ upper 1 m, Agrawal et al. 1992; Terray et al. 1996; Wang et al. 2018). Non-breaking waves influence turbulence through Stokes drift. The vertical shear associated with Stokes drift decays exponentially with depth and acts as a source of turbulence production. Its interaction with the mean ocean current shear reorients vertical vorticity and generates counter-rotating vortices aligned with the wind (Craik and Leibovich 1976; Leibovich 1983), known as Langmuir circulations. These circulations organize the flow into convergence zones and horizontal rolls, often visible as surface windrows (Smith 1992; Kukulka et al. 2009). Evidence from both observations and LES shows that

compared to a wind-forced boundary layer with no waves, Langmuir circulations are associated with enhanced vertical velocities (e.g. Polton and Belcher 2007), turbulence (e.g. McWilliams et al. 1997; Grant and Belcher 2009; D'Asaro et al. 2014; Ferris et al. 2022; Cifuentes-Lorenzen et al. 2024), and turbulent transport (e.g. Gerbi et al. 2009; Kukulka et al. 2012; Chen et al. 2016; Chor et al. 2021; Jarosz et al. 2021).

Since appropriate oceanic measurements of simultaneous forcing and the all the necessary terms of the turbulence kinetic energy budget are not attainable, large-eddy simulations (LES, Skyllingstad and Denbo 1995; Harcourt and D'Asaro 2008; Grant and Belcher 2009; Noh et al. 2011; Kukulka et al. 2012; Large et al. 2019a,b, 2021b; Skyllingstad et al. 2023) have been used to understand the role of Langmuir turbulence in shaping OSBL structure and energetics. Realistically-forced LES more closely reproduce observed boundary layer properties when Langmuir effects are included (e.g., Kukulka et al. 2012; Fan et al. 2020; Skyllingstad et al. 2023; Pham et al. 2023). Further, the incorporation of Langmuir effects into OSBL parameterizations in ocean general circulation models (OGCMs) has reduced the shallow bias in mixed-layer depth (Li et al. 2019). However, substantial differences remain between parameterization schemes, particularly in the Southern Ocean during summer, where Langmuir turbulence is considered important (Belcher et al. 2012; Dong et al. 2024) due to strong winds and persistent wave fields with nearly unlimited fetch that drive intense upper ocean mixing.

A widely used approach for diagnosing OSBL turbulence under neutral forcing is to compare observed dissipation rates (an observable variable) to predictions from the law-of-the-wall. This classic framework assumes steady-state, horizontally homogeneous flow, where surface stress drives a local shear production that is entirely dissipated. Deviations from the scaling can reflect either a breakdown in the underlying assumptions behind the law-of-the-wall or the presence of additional sources or sinks of turbulent kinetic energy (TKE). The law-of-the-wall scaling was extended to include cases where buoyancy forcing has a non-negligible effect on shear production by Monin and Obhukov (MOST Monin and Obukhov 1954) and seminal work by Lombardo and Gregg (1989) illustrated a scaling for dissipation under mixed wind and convective conditions. Several subsequent observation-based studies illustrate deviations from the law-of-the-wall when surface gravity waves become important, specifically pointing towards enhanced or reduced magnitudes of dissipation (e.g. D'Asaro et al. 2014; Sutherland et al. 2014; Esters et al. 2018; Zheng et al.

2021). Accordingly, MOST has been modified to account for Stokes shear (e.g. McWilliams and Sullivan 2000; Smyth et al. 2002; Large et al. 2019a, 2021b). In particular, the assumption of shear production-dissipation balance when overturning cells are present, such as under strong convection or when there are Langmuir cells does not hold. This was demonstrated for the atmospheric surface layer by Wyngaard and Coté (1970), where there is an imbalance between shear production and dissipation due to non-local turbulent transport when large convective cells are present. Under wave forcing non-local transport has also been found to be important and was subsequently incorporated into the similarity scaling framework of Large et al. (1994) either via an additional nonlocal term (e.g. Chor et al. 2021) or through modifications to the structure function (e.g. Large et al. 2019b).

In the Southern Ocean – where effects of wave-driven turbulence might be expected to be large – enhanced dissipation relative to the law-of-the-wall is not consistently observed. For example, in a campaign in the Drake passage, predictions were largely biased low compared to observations (Ferris et al. 2022), however, in two campaigns further to the East, predictions were equal or biased high (Nicholson et al. 2022; Giddy et al. 2023). This, even though all campaigns occurred during austral summer under substantial wave forcing. Interacting factors may explain these differences. Under conditions of wind–wave misalignment (e.g. Van Roekel et al. 2012) or when waves interact with fronts (e.g. VreĆica et al. 2022), Langmuir circulations weaken, and turbulence is reduced below expected levels. Additionally, under conditions of Stokes forcing it has been shown that turbulent transport plays a non-negligible role in the TKE budget throughout the boundary layer (e.g. Gerbi et al. 2009; Kukulka et al. 2012; Chor et al. 2021), violating the local balance of shear production and dissipation that is assumed in the law-of-the-wall.

In this study, we use realistically-forced LES combined with a suite of dissipation rate observations to show how the underlying assumptions of the law-of-the-wall framework break down under wind-wave forcing. Building on this, we propose a modified similarity scaling that incorporates non-local TKE transport, offering a more physically grounded approach to the application of similarity-scaling in wave-forced ocean boundary layers.

Section 2 summarizes the relevant similarity scaling theory; Section 3 describes the data and methods. In Section 4, we analyze similarity scaling relative to resolved turbulence in realistically-forced LES and introduce a modified framework. Section 5 compares various scaling approaches to observations, and Section 6 discusses the broader implications.

2. Theoretical Framework

a. Turbulent Kinetic Energy

The velocity of a turbulent flow can be split into a mean flow and a fluctuating flow ($\mathbf{U} = \overline{\mathbf{u}} + \mathbf{u}'$). Turbulent Kinetic Energy (TKE) is the kinetic energy per unit mass associated with the fluctuating flow. For a horizontally homogeneous flow, no mean advection, and assuming a rigid lid where the effects of surface gravity waves are omitted:

$$\partial_t \mathrm{TKE} = -\langle w'\mathbf{u}'\rangle \cdot \partial_z \mathbf{U} + \langle w'b'\rangle + \mathrm{transport} - \varepsilon \tag{1}$$

where ∂_tTKE is the rate of change of TKE, $\langle\rangle$ denote time and/or horizontal space averaging, primed values turbulent fluctuations, and b is buoyancy, with $b = -g\frac{\rho}{\rho_0}$, where ρ is the seawater density and ρ_0 is a reference density. We use a right-handed Cartesian coordinate system with z increasing upward. The first term on the right-hand side represents the production of TKE through the vertical shear of mean horizontal currents, $\mathbf{U}$, the Eulerian shear. The second term is the turbulent buoyancy flux, which is negative and a sink of TKE under stabilizing surface buoyancy forcing and positive and a source of TKE under destabilizing surface buoyancy forcing. The transport term represents divergence of TKE transport – hereinafter 'TKE transport' – due to turbulent fluctuations of the vertical velocity and pressure. The final term, ε, represents the rate of destruction of TKE due to viscosity (turbulence dissipation).

b. Similarity Theory

Semi-empirical Monin-Obukhov similarity theory (MOST, Monin and Obukhov 1954; Wyngaard 2010; Foken 2006) provides a framework for describing planetary boundary layers under horizontally homogeneous and stationary conditions, assuming a rigid-lid boundary. It relates turbulent quantities to distance from the surface, $|z|$, using only the surface forcing parameters.

The boundary layer of thickness h, taken as the actively mixing layer in contact with the surface, includes the viscous sublayer directly influenced by the surface (~0.01-0.03h), the surface layer, and the bulk of the boundary layer. Across all observations and simulations analysed in this study we identify h as the first depth from the surface where $\varepsilon \leq 10^{-8}$ m^2 s^{-3} (Brainerd and Gregg 1995). The surface layer is defined as the layer extending from the viscous sublayer to 10% of the height

of the boundary layer ($0.1h$). Within this layer, the turbulent momentum and buoyancy fluxes are approximately constant. Surface forcing is characterized by the friction velocity, $u_* = \sqrt{\frac{\tau}{\rho_0}}$, where $\boldsymbol{\tau}$ is the magnitude of the turbulent surface stress vector, and by the surface buoyancy flux, B_0, from which we define the buoyancy forcing scale $b^* = B_o/u_*$. The turbulent stress is related to the turbulent momentum flux via $\boldsymbol{\tau} = -\rho_0 \langle w' \mathbf{u}' \rangle$. In MOST, the vertical shear and stratification profiles, characterized by the friction velocity and the surface buoyancy flux respectively, become functions of a single dimensionless group - the stability parameter - which depends on z and the Monin-Obukhov length scale, L (Wyngaard 2010).

$$\zeta = \frac{z}{L} = \frac{\kappa z B_o}{u_*^3}, \tag{2}$$

with

$$L = \frac{u_*^3}{\kappa B_o}, \tag{3}$$

where $\kappa = 0.4$ is the universal von Kárman constant and L defines the depth at which the shear production of turbulence balances buoyancy production.

The non-dimensional shear is given as,

$$\Psi_m = \frac{\kappa z}{u_*} \partial_z U = \phi_m(\zeta), \tag{4}$$

determined experimentally in atmospheric boundary layers under unstable conditions as a function of the stability parameter (Businger et al. 1971; Hogstrom 1988) and fine-tuned to the Southern Ocean using LES (Large et al. 2019a):

$$\phi_m = (1 - 14\zeta)^{-1/3}. \tag{5}$$

Assuming all shear production is generated by mechanical forcing at the surface of the ocean and buoyancy is negligible such that $\Psi_m = \phi_m(\zeta) = 1$, the classic law-of-the-wall scaling for the shear production of turbulence emerges where:

$$-\langle w'\mathbf{u}'\rangle \cdot \partial_z \mathbf{U} = u_*^2 \left[\frac{u_*}{\kappa|z|}\right]. \tag{6}$$

Under certain conditions (e.g. wind driven shear production), this scaling can be applied below the surface layer (i.e., beyond $0.1h$) but requires assuming a model (often linear) for how the turbulent stress decays to zero at the base of the boundary layer (Stull 1988; Watkins and Whitt 2020; Zippel et al. 2022; Zeiden et al. 2024) and that the stress aligns with the shear at all depths.

$$-\langle w'\mathbf{u}'\rangle = u_*^2 \left[1 - \frac{|z|}{h}\right], \tag{7}$$

giving:

$$-\langle w'\mathbf{u}'\rangle \cdot \partial_z \mathbf{U} = u_*^2 \left[1 - \frac{|z|}{h}\right]\left[\frac{u_*}{\kappa|z|}\right], \tag{8}$$

The ocean surface boundary layer differs from the atmospheric boundary layer in two ways. First, the coupling between the speed of the bulk fluid and the stress u_* differs since u_* is mainly defined by the wind in both cases. The ocean thus permits greater decoupling between the bulk current speed and the stress and the surface layer shear - the latter two of which similarity posits are tightly coupled and analogous in both atmospheric and ocean cases. Secondly, and the focus of this study, is the presence of surface gravity waves that introduce an additional source of turbulence production not captured by MOST. In particular, the interaction between wind and waves drives Langmuir turbulence, which requires modifying the similarity framework to include wave effects.

1) Langmuir turbulence

Langmuir turbulence can be described through the Craik-Leibovich wave-averaged equations (Craik and Leibovich 1976), with Stokes drift an imposed forcing (McWilliams et al. 1997; Belcher et al. 2012), which results in an additional term in Eq. 1 - Stokes shear production:

$$\partial_t \mathrm{TKE} = -\langle w'\mathbf{u}'\rangle \cdot \partial_z \mathbf{U} - \langle w'\mathbf{u}'\rangle \cdot \partial_z \mathbf{U_s} + \langle w'b'\rangle + \mathrm{transport} - \varepsilon, \tag{9}$$

where Stokes shear production is $-\langle w'\mathbf{u}'\rangle \cdot \partial_z \mathbf{U_s}$.

Large et al. (2019a) (herafter L19) build on the MOST framework to develop a turbulent velocity scaling that includes the effects of Stokes drift and Langmuir turbulence, taking Stokes drift as an independent surface forcing. L19 introduce a second non-dimensional function to Eq. 4, the Stokes similarity function, a function of the Stokes parameter, ξ, representing the proportion of Stokes production of TKE to the total production of TKE (the sum of shear production, Stokes shear production and buoyancy production), such that:

$$\Psi_m = \phi_m(\zeta)\chi_m(\xi), \tag{10}$$

with $\chi_m(\xi)$ an empirically defined function fit to L19 LES output as:

$$\chi_m = 1.05 + 2.43\xi + 1.69\xi^2, \tag{11}$$

where

$$\xi = \frac{\mu_s^3}{\mu_u^3 + \mu_s^3 + \mu_b^3}, \tag{12}$$

and $\mu_u^3 = P_u u_*^3$, $\mu_s^3 = P_s \mathrm{La}^{-2} u_*^3$, $\mu_b = P_B w_*^3$ defining the cubes of three velocity scales for the surface forcing. The turbulent Langmuir number is defined as $\mathrm{La} = \sqrt{\frac{u_*}{U_s}}$ (McWilliams et al. 1997), where $\mathrm{La} \leq 0.3$ indicates wave-driven turbulence conditions, and $w_*^3 = -B_o h$ defines the convective velocity scale. The empirically derived parameters, P_u, P_s, are based on turbulence and forcing in the L19 LES, with $P_B = 0.09$. This empiricism is needed as the surface forcing given by u_*, w_* and La do not account for all the variability in TKE production in the surface layer. The parameters defined in L19 are specific to $0.1h$, but L19 shows that χ_m is depth invariant at least to $0.25h$ (their Figure 6a).

Using the stability parameter ζ and the Stokes parameter ξ defined above, the Eulerian shear is scaled to account for both Stokes and surface buoyancy forcing. Thus the law-of-the-wall scaling for shear production given in Eq. 6 can be extended for unstable, wavy conditions:

$$-\langle w'\mathbf{u}'\rangle \cdot \partial_z \mathbf{U} - \langle w'\mathbf{u}'\rangle \cdot \partial_z \mathbf{U_s} = u_*^2 [1 - \frac{|z|}{h}] \left[\phi_m(\zeta)\chi_m(\xi) \frac{u_*}{\kappa |z|} + \partial_z \mathbf{U_s} \right]. \tag{13}$$

198 2) Turbulence dissipation

199 Under the assumptions of stationarity, negligible turbulent transport, neutral buoyancy forcing
200 and the absence of surface gravity waves, the shear production of TKE is locally balanced by
201 dissipation:

$$\varepsilon = -\langle w'\mathbf{u}'\rangle \cdot \partial_z \mathbf{U}. \tag{14}$$

202 This relation forms the basis for approximating turbulence dissipation using the MOST framework
203 (the law-of-the-wall approximation under neutral buoyancy forcing - Eq. 6 and its extensions
204 (Eq. 7-8).

205 However, under neutral conditions and in the presence of surface waves, two modifications need
206 to be accounted for: 1) a shear term associated with Stokes drift and 2) the vertical transport of
207 TKE which becomes non-negligible (Gerbi et al. 2009; Polton and Belcher 2007; Kukulka et al.
208 2012), as under strong destabilizing conditions (Wyngaard and Coté 1970). Although this transport
209 term redistributes TKE vertically and integrates to zero over the full boundary layer, it modifies
210 the local TKE balance and must be explicitly considered when predicting dissipation profiles.

211 Thus, for neutral buoyancy with both wind and wave forcing, and no significant TKE tendency,
212 ∂tTKE, the local dissipation rate reflects contributions from Eulerian shear production, Stokes
213 shear production, and the vertical transport of TKE

$$\varepsilon = -\langle w'\mathbf{u}'\rangle \cdot \partial_z \mathbf{U} - \langle w'\mathbf{u}'\rangle \cdot \partial_z \mathbf{U_s} + \text{transport}. \tag{15}$$

214 Under conditions of pure wind forcing, it can be assumed that the stress and shear components
215 of the shear production term are aligned. However, under the presence of waves, stress and shear
216 are often misaligned (Van Roekel et al. 2012).

217 We define the magnitude of alignment between the stress and shear components as Θ, the
218 normalized dot product of the stress and shear, which can be interpreted as the cosine of the angle
219 between the stress and shear vectors such that a value of one indicates that the stress and shear are
220 aligned.

$$\Theta_E = -\frac{-\langle \mathbf{u}'w'\rangle \cdot \partial_z \mathbf{U}}{|\langle \mathbf{u}'w'\rangle||\partial_z \mathbf{U}|}, \tag{16}$$

$$\Theta_S = -\frac{-\langle \mathbf{u}'w' \rangle \cdot \partial_z \mathbf{U_S}}{|\langle \mathbf{u}'w' \rangle||\partial_z \mathbf{U_S}|}. \tag{17}$$

With this, the Eulerian shear production can be represented as:

$$-\langle \mathbf{u}'w' \rangle \cdot \partial_z \mathbf{U} = \Theta_E |\langle \mathbf{u}'w' \rangle||\partial_z \mathbf{U}_E|, \tag{18}$$

and Stokes shear production as:

$$-\langle \mathbf{u}'w' \rangle \cdot \partial_z \mathbf{U_S} = \Theta_S |\langle \mathbf{u}'w' \rangle||\partial_z \mathbf{U}_S|. \tag{19}$$

L19 provides a framework for approximating Eulerian shear production under buoyancy and wave forcing, but does not extend their results to directly predict turbulence dissipation rates and thus did not consider non-local transport in their framework. While the qualitative contribution of transport has been considered in a number of studies (e.g Gerbi et al. 2009; Polton and Belcher 2007; Kukulka et al. 2012; Chen et al. 2016; Chor et al. 2021), its quantitative contribution to turbulence dissipation remains poorly constrained, particularly in observations.

3. Description of Large Eddy Simulations and Observational data

a. Study Sites

The observations and simulations described in this study are from three regions of the Southern Ocean (Fig. 1a): 1) the Subantarctic Zone (SAZ; glider deployed at 42°S, 0°E and LES initialized and forced with conditions at the Southern Ocean Flux Site, 46°S, 142°E, (Schulz et al. 2012), 2) the Antarctic Polar Frontal Zone (APZ; glider deployed at 54°S, 0°E), and 3) within the Seasonal Ice Zone (SIZ; glider deployed at 60°S, 0°E) - a region that is covered by sea ice in the winter and experiences open ocean conditions during summer. The boxes in Figure 1 identify the regions where the gliders were deployed and the location of the SOFS mooring, whose oceanic and forcing conditions informed the LES. For scale, the gliders were piloted in bow-tie patterns of 20-40 km except for the SAZ glider which maintained a mooring sampling pattern with each surfacing approximately 4 hours apart. The LES horizontal domain was 1250 x 1250 m and 300 m in the vertical.

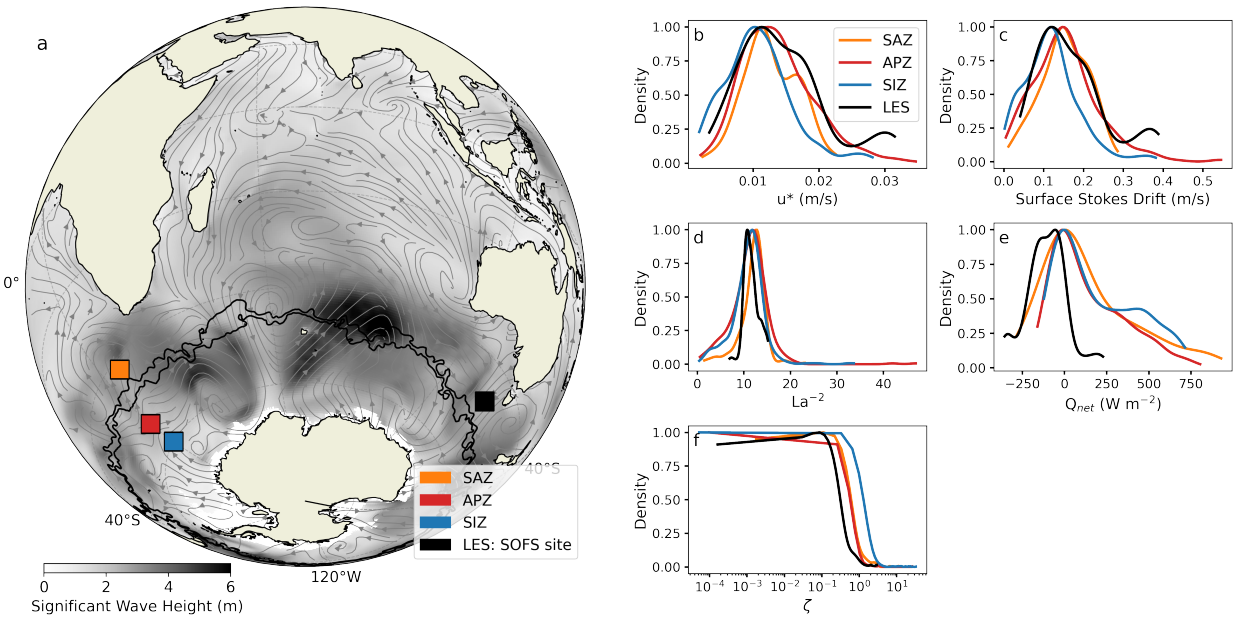

FIG. 1. a) Locations of Large Eddy Simulations (black: Southern Ocean Flux Site, 46°S, 142°E), and three glider-Microrider deployment sites (orange: Subantarctic Zone, 42°S,7°E; red: Polar Frontal Zone, 64°S, 0°E; blue: Seasonal Ice Zone, 60°S, 0°E). Grey color scale shows the mean ERA5 Significant Wave Height for January 2019, with streamlines of ERA5 wind speed at 10m for the same time period. Solid black contours indicate the mean location of the Subantarctic Front (northern contour, 0 absolute dynamic topography (ADT) contour) and and Antarctic Polar Front (southern contour, -0.3 ADT) during the same period (Sallée et al. 2008). (b-e) The distributions of the forcing conditions at each of the study sites: b) Friction velocity, c) Surface Stokes Drift, d) Turbulent Langmuir Number, $\mathrm{La}^{-2} = \frac{U_s}{u_*}$, e) Net Heat Flux and f) Stability parameter, ζ.

These regions are hydrographically distinct in water mass structure (Du Plessis et al. 2022), however the surface forcing that they experience during the time of sampling is similar, dominated by strong wind and wave forcing with net buoyancy flux into the ocean on average (Fig. 1b-f). The LES runs were forced with stronger destabilizing buoyancy fluxes (net flux out of the ocean that occurred during austral autumn, April and June) compared to the glider observations (taken during austral summer, December-February, Fig. 1e). For the purpose of this study, we subset the data for destabilizing conditions in both observations and LES. Wind-wave conditions are typically fully developed (Fig 1f, e.g. $\mathrm{La}^{-2} \sim 11$, Belcher et al. 2012; Large et al. 2019a) and buoyancy forcing is weak compared to shear ($|\zeta| = |\frac{z}{L}| \leq 1$, where z is taken at 10 m).

b. Large Eddy Simulations

Realistically-forced LES solutions of the ocean boundary layer representing conditions at the Southern Ocean Flux Site (SOFS) with and without the surface wave effects encapsulated in the wave-averaged Craik-Leibovich equations during April and June of 2010 are used in this study (Large et al. 2021a). This NCAR LES model is well documented (Moeng 1984; Sullivan et al. 1994; McWilliams et al. 1997). Modifications to the model to account for realistic surface wave effects are given by Large et al. (2019a) which has been used to study wave forced Southern Ocean conditions by Large et al. (2019a,b, 2021b). The model solves the wave-averaged, incompressible, and Boussinesq Craik-Leibovich equation set (Craik and Leibovich 1976; McWilliams et al. 1997). The computational domain spans a horizontal area of 1250×1250 m with a mesh grid of 1280×1280 cells. This configuration provides a fine horizontal resolution of approximately 1 m. The vertical grid configuration differs between the two simulation periods. For the April simulations, the domain reaches a vertical extent of 300 m; resolution starts at 0.375 m at the surface and stretches to 1.13 m at the base. The June simulations utilize a vertical extent of 500 m with a surface resolution of 0.376 m stretching to 2.02 m at the base. Both simulations use a stretching factor of $r = 1.0035$. In both cases, the vertical resolution is sufficient to resolve the rapid vertical decay of Stokes drift. The time steps are set to 0.9 s for the April simulations and 1.5 s for the June simulations. Further details are provided in Section 3, Table 1 of Large et al. (2019a). We use half hourly profiles of horizontal and time mean Eulerian flow and buoyancy with corresponding turbulent vertical fluxes, which include the correlations of vertical velocity w' with fluctuations, b', u' and v', plus subgrid scale (SGS) contributions (which are small except near the surface boundary). Profiles of Stokes drift are imposed as forcing. Variance of velocity fluctuations plus SGS give the TKE, whose dissipation ε is parameterized (that is, throughout this manuscript we refer to the dissipation of subgrid TKE as dissipation). The turbulent transport is determined as the residual term in the TKE budget, assuming steady state conditions, by subtracting dissipation from the sum of the Eulerian shear production, Stokes shear production and buoyancy production.

The Southern Ocean surface conditions based on SOFS in April and June are, on average characterized by a buoyancy flux negative out of the ocean, with equilibrium winds and waves ($\mathrm{La}^{-2} = 11$). The forcing varies over the 50 hours in which the LES are run, ranging between strong winds ($\sim$20 m s^{-1}) and quiescent conditions and similarly stronger convection ($\sim$200 W m^{-2}) to

neutral buoyancy forcing, including one instance of stabilizing positive surface buoyancy forcing into the ocean (see Fig. A1). For a detailed breakdown of the LES into different regimes see Table 2 of Large et al. (2019a). We are interested in analyzing the turbulence that is relatively well developed and near steady state, so we isolate those periods of the LES when the boundary layer is forced by relatively strong and consistent winds, near wind-wave equilibrium, and only modestly convective for analysis. Of the 50 simulated hours in April, we exclude $t = 23 - 31$ hours (when the winds are weak and rotating), and of the 41 simulated hours in June, we exclude the first 12 hours and $t = 33 - 41$ hours (when convection is dominant and winds are weak and rotating) (see Appendix A1, Fig. A1 - gray line coloring delineates the regimes that we exclude).

The LES with Stokes forcing resolve coherent downward vertical velocities roughly aligned with the wind characteristic of Langmuir circulations - about 100 m wide, up to 800 m long and separated by more than 300 m (see Large et al. 2019a, their Figure 4). Upwelling cells fill a broader area, characteristic of convective cells. Inertial oscillations are present in both Stokes and no Stokes cases, visible through the ~15 hour oscillations in the averaged mean velocities, characteristic of the inertial period at this latitude (see A1). Internal tides that are present in the real ocean are not simulated and there are no mean lateral buoyancy gradients (fronts).

c. Microstructure shear observations and derivation of turbulence dissipation

Observations of turbulence dissipation are calculated from profiles of microstructure shear from three deployments of a Slocum glider during SOSCEx-STORM experiments (Swart et al. 2012; Nicholson et al. 2022). The experiments occurred in the SAZ (21 December 2017-17 January 2018; 42°S,7°E), the APZ (19 December 2018-8 March 2019; 54°S,0°E) and the SIZ (17 December 2019-23 January 2020; 60°S,0°E) over consecutive years (2017-2019) during austral summer, resulting in a total of 1220 profiles (see Fig. B1).

Microstructure data were collected using the self-contained turbulence instrument package MicroRider-1000LP (MR, Rockland Scientific International, Canada). The MR was attached to the top of a Slocum glider with turbulence sensors protruding at the front, and was equipped with two airfoil velocity shear probes (SPM-38) oriented orthogonal to each other such that the first shear probe was sensitive to perturbations in the vertical, and the second shear probe was sensitive to perturbations in the horizontal direction relative to the direction of

travel of the glider ($\partial w/\partial x$ and $\partial v/\partial x$ respectively). For processing the microstructure shear additional sensors are required: a pressure transducer, a two-axis vibration sensor (a pair of piezo-accelerometers), and a high-accuracy dual-axis inclinometer (ADIS 16209, pitch and roll angles accurate to 0.18°). Shear microstructure measurements were made to at least 500 m on both climbs and dives during the SAZ and the SIZ deployments, while during the APZ deployment, the MR was only powered on during climbs. The sampling frequency is 512 Hz on all turbulence channels (vibration, shear) and 64 Hz for the other channels (pitch, roll, and pressure).

The dissipation rate of TKE (dissipation hereinafter) is estimated by integrating the shear wavenumber spectrum, assuming isotropic turbulence:

$$\varepsilon_j = \frac{15}{2}\nu\left\langle\left(\frac{\partial u_j}{\partial x}\right)^2\right\rangle \approx \frac{15}{2}\nu\int_{k_l}^{k_u} S'(k)dk, \tag{20}$$

where $\frac{\partial u_j}{\partial x}$ is the turbulent scale shear component measured along the glider's along-path coordinate x, and j identifies the shear probe number oriented orthogonal to measure the transverse ($\partial v/\partial x$) and vertical ($\partial w/\partial x$) components of the along-path shear. The kinematic viscosity of seawater, ν, is a function of the local water temperature. The shear wavenumber spectrum S', is integrated between k_l, set by the window length and k_u, the minimum in a curve fit to the shear spectrum, that is unaffected by noise. The dissipation estimates are obtained following Fer et al. (2014) and the recommendations of the SCOR Working Group on analysing ocean turbulence observations to quantify mixing (ATOMIX, Lueck et al. (2024)). Following the initial estimation of dissipation a number of quality control steps were applied. Further details on the processing and QC of the microstructure shear data are described in Giddy et al. (2025). Due to glider surface maneuvers reliable estimates of dissipation rate start at 10 m during dives and below 3-5 m for climbs. Finally, the glider dataset is regridded to 1 m depth bins in the vertical. Each dive and climb is then treated as a single profile and allocated a timestamp that represents the average time during that dive.

d. Surface forcing

Similarity scaling of turbulence in the ocean surface boundary layer relies on knowledge of the surface forcing from which the structure of the boundary layer is approximated. Key turbulent

fluxes are the momentum flux and the buoyancy flux. The third variable in the case of wave forcing is Stokes drift.

The LES are forced with observations from the SOFS mooring and the time-varying wave effects (2D wave spectra from which Stokes drift is computed) are generated from the wave prediction model, WAVEWATCH III (Tolman 2009), initialized with ECMWF wave spectra.

To interpret the microstructure shear observations, we use the ECMWF Reanalysis v5 hourly reanalysis product, ERA5 (Hersbach et al. 2020, 2023) for surface buoyancy fluxes and wind stress and the ECWMF WAM global wave model (ECMWF 2013) for Stokes drift in lieu of co-located in situ measurements of winds, waves and buoyancy during the full time periods of the glider deployments. We choose to use the ECMWF WAM model when interpreting the dissipation observations for consistency with ERA5 surface forcing. Even though two different wave models are used in this study (WAVEWATCH III in the LES and ECMWF WAM together with the dissipation observations) differences in Stokes drift profiles between WAVEWATCH III and ECMWF WAM are expected to be small (e.g. Swain et al. 2019).

The atmospheric component of ERA5 has a horizontal resolution of approximately $0.25° \times 0.25°$. The 2-dimensional wave variance spectrum that describes how the mean sea-surface elevation variance due to ocean waves is distributed as a function of frequency and propagation direction is given hourly at a resolution of approximately $0.5° \times 0.5°$.

Stokes drift was shown by Kenyon (1969), in the case of linear waves, to relate to the wave variance density spectrum $E(\omega,\theta)$. The circular frequency, $\omega = 2\pi f$, can be transformed to, f, the linear frequency using a simple coordinate transform giving a description of Stokes drift as a function of linear wave frequency and direction (Breivik et al. 2014):

$$\mathbf{U}_s(z) = \frac{16\pi^3}{g} \int_0^{2\pi} \int_0^{\infty} f^3 \hat{\mathbf{k}} e^{2kz} F(f,\theta) df d\theta, \tag{21}$$

where θ is measured clockwise from north and $\hat{\mathbf{k}}(f,\theta) \equiv \mathbf{k}/|\mathbf{k}|$ is the normalized direction vector of the wave component. The Stokes drift profile was computed from the full 2D spectrum following Eq. 21. A diagnostic f^{-5} tail was added to the spectrum beyond the cutoff frequency. This has a significant impact on the surface Stokes drift (up to 30%, see Breivik et al, 2016). The effect of high-frequency waves vanishes quickly with depth, creating a strong gradient in the Stokes drift

profile in the upper part of the boundary layer.

In the case of the LES, wind stress magnitude, τ, is derived from wind speeds observed at the SOFS mooring using the COARE 3.0 bulk formulation (Fairall et al. 2003). For the wind stress applied to the observed dissipation we use ECMWF, which is calculated by the ECMWF Integrated Forecasting System's turbulent diffusion and turbulent orographic form drag schemes (ECMWF, 2019).

The net surface buoyancy flux into the ocean is given by:

$$B_o = g\left[\frac{\alpha Q_{net}}{\rho_0 c_p} - \beta S(E-P)\right], \tag{22}$$

where $g = 9.81$ m s^{-2} is the gravitational acceleration, α is the thermal expansion coefficient and β is the haline contraction coefficient both computed from surface Absolute Salinity (S) and Conservative Temperature measured by the Slocum glider, using the Gibbs SeaWater TEOS-10 Toolbox (McDougall and Barker 2011), Q_{net} is the net heat flux into the ocean (shortwave + longwave + latent + sensible), c_p is the heat capacity of water = 3991.9 J K^{-1} kg^{-1}, ρ_0 = 1027 kg m^{-3} is a reference seawater density, and E and P, are the evaporation and precipitation rates, respectively.

As wind and wave variables are computed from a model we acknowledge that the surface forcing as derived here from ERA5 may not be fully consistent with the observations. However, comparison with the co-located in situ wind observations from a Waveglider from part of the deployment show agreement with wind speed variability from ERA5, with ERA5 tending to underestimate the mean by 10-20%, although we note that the energy containing wind forcing is well resolved (see Fig. B2).

4. Similarity functions of Turbulence Kinetic Energy in No Stokes and Stokes LES

A key term in the TKE equation (Eq. 1) is the shear production term. Momentum at the ocean surface is transported to depth by turbulent eddies generated via shear production. This is the process that is parameterized in OGCMs as a turbulent viscosity term that is based on an understanding of shear production. Furthermore, turbulence generation by shear production, under neutral buoyancy forcing, is the primary source of energy that is ultimately dissipated, and thus

relates directly to observations of turbulence dissipation rate. In the following, we describe an example of shear production under wind only and wind-wave forced conditions in the realistically forced LES. We then statistically assess the shear production and dissipation of the LES runs compared to scaling parameterizations with the intention to understand the link between shear production and dissipation. Our interest is primarily in the surface layer (above $0.1h$), but we analyze depths down to $0.25h$.

a. Example of the vertical structure of shear production under wave forcing from an LES

Under neutral stratification and no buoyancy forcing, assuming constant momentum flux, and a rigid lid, the law-of-the-wall scales shear production as a function of friction velocity and distance from the boundary (Eq. 6). Fig. 2 decomposes the terms in the law-of-the-wall scaling (Eq. 6) and compares them to LES solutions of the Craik-Leibovich wave-averaged equations (Eq. 9) for TKE under pure wind forcing and wind-wave forcing. First consider pure wind forcing. Shear production (Fig. 2d) is the dot product of a vertical turbulent momentum flux (Fig. 2a) and a vertical shear (Fig. 2b). Friction velocity squared (u_*^2) is equivalent to the LES vertical turbulent momentum flux ($-\langle \mathbf{u}' w' \rangle$) at the ocean surface. In the LES, the vertical turbulent momentum flux generally decays to zero at the base of the boundary layer (as seen in the snapshot in Fig. 2a), while in the law-of-the-wall, the parameterized momentum flux is constant with depth - a good approximation between the surface and $0.1h$. Vertical shear is represented as $\frac{u_*}{\kappa|z|}$ in law-of-the-wall. Under pure wind forcing the law-of-the-wall accurately reproduces the LES shear down to $z \sim 0.8h$. Under pure wind forcing, Θ_E, shown in Fig. 2c is close to 1 throughout the surface layer, indicating stress aligned with shear. The law-of-the-wall and LES shear production are compared in Fig. 2d. Near the surface, law-of-the-wall is representative of shear production in the LES. The quality of the law-of-the-wall fit to LES decays with depth. This is partly due to a failure in the assumption of constant momentum flux away from the boundary as seen in Fig. 2a. Using a linear decay in momentum flux, $u_*^2[1 - \frac{|z|}{h}]$, (Eq. 7), in place of a constant momentum flux, u_*^2, significantly improves the representation of shear production below $0.1h$ for the pure wind forcing case. At the LES simulation latitude of 47°S, planetary rotation may significantly affect the turbulent stress within the boundary layer (e.g., Zikanov et al. 2003; Liu et al. 2018). Turbulent momentum stress is constrained by the Ekman spiral which results in a counterclockwise veering of momentum with

depth in the Southern Hemisphere (not shown) and suppression of the stress. The stress profiles shown in the example Fig 2a and e are qualitatively consistent with rotational effects in wind only and wind-wave affected boundary layers. The boundary layer depth is 179 m and 181 m for No Stokes and Stokes cases, with an Ekman depth of 206 m (giving a scaled Ekman depth of -1.1). Under Stokes forcing, the effect of Coriolis on the stress profile tends to be reduced due to the increased mixing by Langmuir turbulence (Fig 2e).

Now consider the Stokes forcing case (Fig. 2e-g). Turbulent momentum flux is well represented by the slab parameterization for momentum flux (similar to the pure wind case). Vertical shear, however, is no longer well represented by $\frac{u_*}{\kappa|z|}$. Vertical shear with Stokes forcing comprises Eulerian shear and Stokes shear with the majority of the shear near the surface attributed to Stokes shear - which arises from different (wave) physics than the $1/z$ form of the wind-driven Eulerian shear arising from law of the wall physics. A substantial angle difference is present between the stress and shear (Fig. 2g). Nevertheless, near the surface, the total shear production parameterized by law-of-the-wall represents the shear production solved by the LES (Fig. 2d,h). This example shows that law-of-the-wall provides a first approximation of shear production in the surface layer of the surface boundary layer in both pure wind and Stokes forcing conditions. In other words under realistic forcing conditions (such as the ones represented here), surface-layer shear production under wind forcing is not necessarily different in magnitude from surface-layer shear production under wind and wave forcing. In the next two sections, we show that this anecdotal example in Fig. 2 is in fact representative of the LES solutions across a broad range of forcing regimes.

Note that in both No Stokes and Stokes cases, shear production deviates from the slab parameterization below the surface-layer. These deviations could be resulting from inadequately accounting for depth dependence such as with the structure functions of Large et al. (1994) and Large et al. (2019b), which are not accounted for here, as well as other processes that modify vertical shear and become relatively more important deeper in the boundary layer - such as shear related to inertial oscillations.

b. Shear production and dissipation dependence with depth

We evaluate the relationship between shear production and dissipation given by the realistically-forced LES compared with the three shear production parameterizations described in section 2 (the

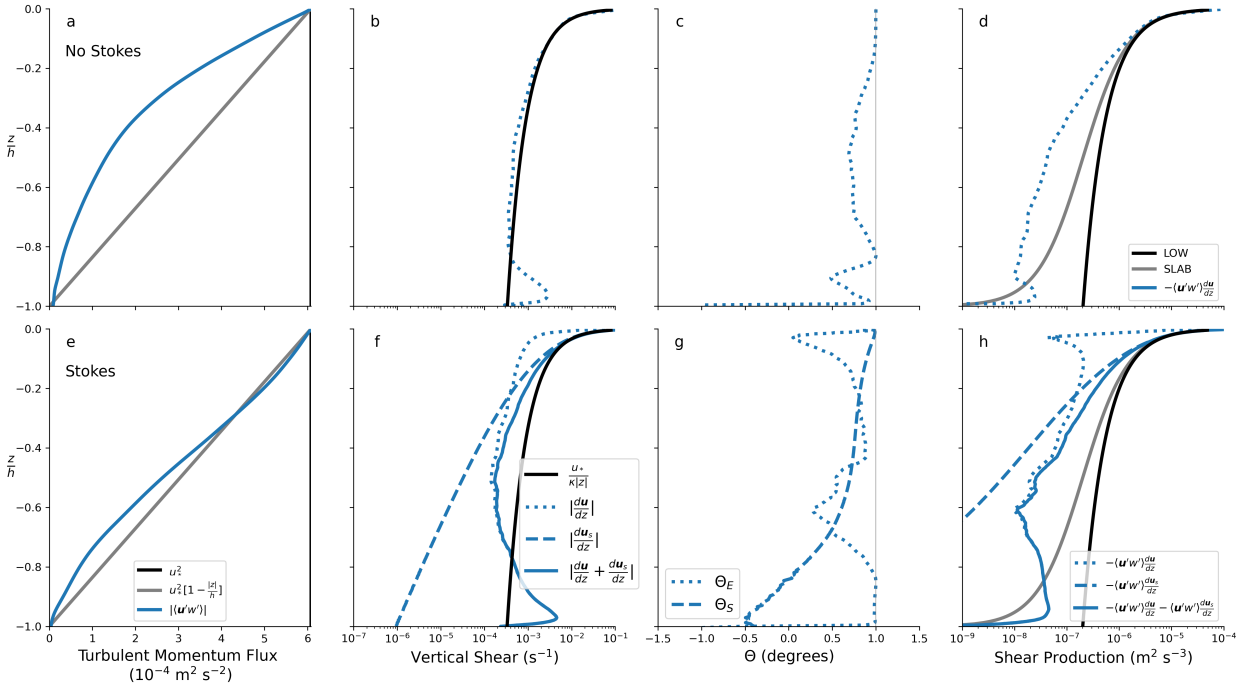

454 FIG. 2. Example of shear production in the surface boundary layer for No Stokes (a-d: top panel) and Stokes
455 forcing (e-h: bottom panel). The black lines represent terms in the law-of-the-wall scaling. The grey lines
456 replace the vertical turbulent momentum flux with a slab model. The blue lines are snapshots of data from the
457 April LES runs of L19 at t=10 hours. (a,e) Magnitude of the vertical turbulent momentum flux; (b,f) Magnitude
458 of Eulerian vertical shear $\frac{d\boldsymbol{u}}{dz}$ (blue dotted lines), and Stokes vertical shear $\frac{\boldsymbol{u_s}}{dz}$ (blue dashed lines), total shear
459 (blue solid line) and wall scaling (black solid line) (c,g) cosine of the angle between the stress and shear vectors
460 and (d,h) shear production. In the No Stokes case, the boundary layer depth is 179 m. In the Stokes case, the
461 boundary layer depth is 181 m.

472 classic wall-scaling, Eq. 6; the slab wall-scaling, Eq. 8; and L19, Eq. 13) with No-Stokes and Stokes
473 cases in April and June (Fig. 3a,b). Recall that the wall-scaling and the slab wall-scaling applied
474 here assume a local balance between shear production and dissipation (Eq. 14), however the TKE
475 budget under steady state also includes a turbulence transport term and a buoyancy flux. Under
476 wind-driven shear conditions transport is assumed negligible, but the same assumption cannot be
477 made under conditions where vertical velocities and thus turbulent transport become important
478 (as in cases of strong convection or Langmuir circulations, Wyngaard and Coté 1970; Polton and
479 Belcher 2007). We illustrate the role of turbulence transport in Fig. 3. The left panels in Fig. 3 show

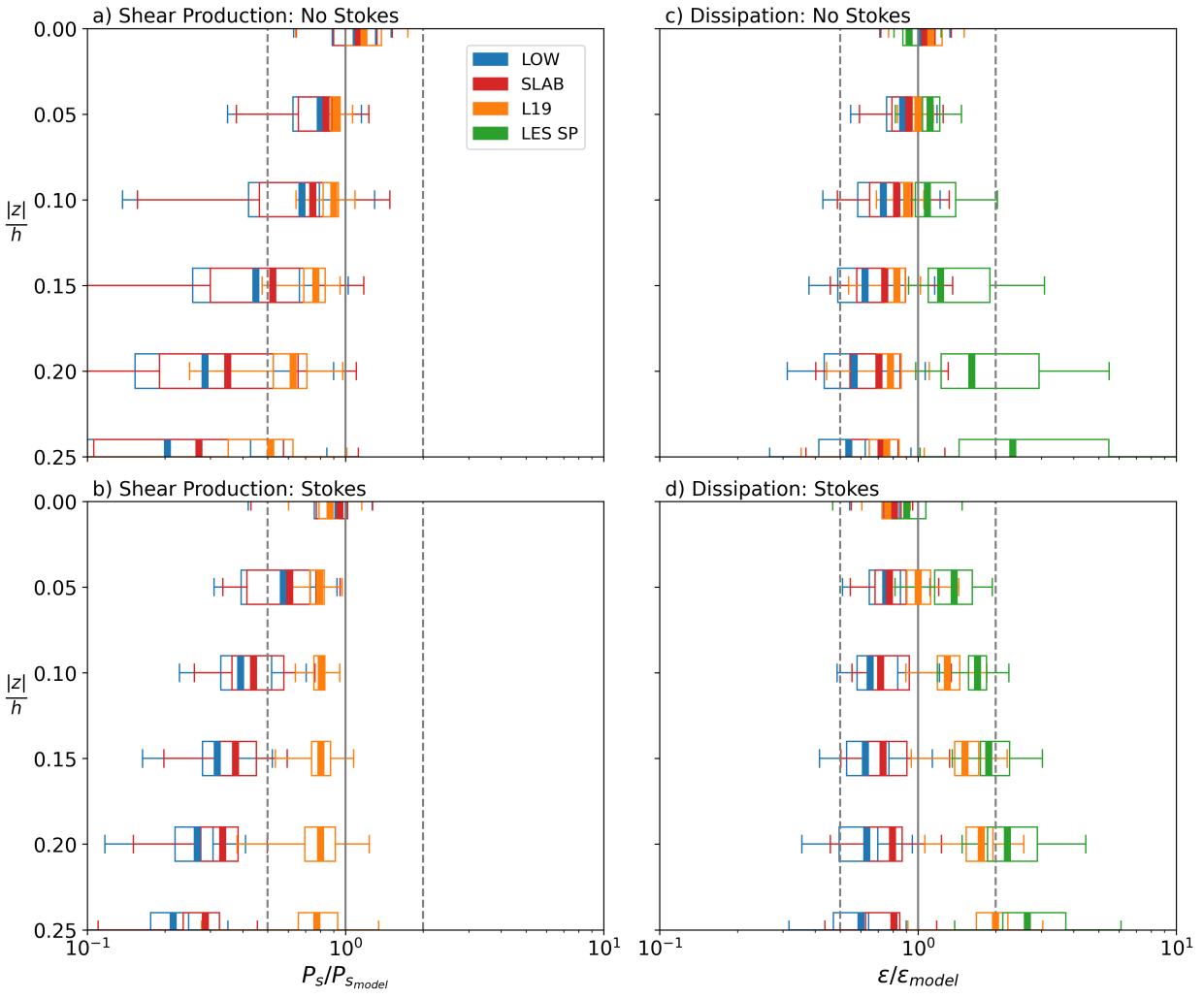

FIG. 3. Box and whisker plots of shear production from L19 No Stokes (a) and Stokes (b) LES runs, scaled by P_S model and ϵ_{model}, where 'model' refers to parameterization after (blue) law-of-the-wall (Eq. 6), (red) slab wall-scaling (Eq. 8), and (orange) Large et al. (2019a) shear production parameterization (Eq. 13). No Stokes (c) and Stokes (d) turbulence dissipation scaled by the same parameterizations for shear production, and additionally in green, LES dissipation scaled by LES shear production. Data are binned by non-dimensional depth ($|z|/h$, where h is the depth of the boundary layer). The solid grey line identifies a 1:1 agreement and the dashed grey lines show factor of two differences. Note the x-axis is in log-scale.

the ratio of LES shear production (LES SP) to parameterized shear production with depth. The right panels show the ratio of LES dissipation (LES ε) to parameterized dissipation with depth. A ratio of one indicates that the parameterization agrees with the simulation. L19 best represents the shear

production in both No Stokes (Fig. 3a) and Stokes (Fig. 3b) forcing cases as it incorporates the effects of waves and buoyancy on Eulerian shear as well as a depth decaying turbulent momentum flux. In the pure wind-driven framework, dissipation is assumed to locally balance shear production. We test this assumption by comparing the same three shear production parameterizations with dissipation. In the No Stokes case, of all three shear production parameterizations L19 most closely matches the LES (i.e., is nearest to 1:1) down to $\sim 0.15h$ (Fig. 3b). In the Stokes case, the L19 shear production parameterization (Fig. 3b, orange) increasingly underestimates the turbulence dissipation with depth, while the law-of-the-wall and slab wall-scaling better represent the dissipation rate (Fig. 3d).

In addition to turbulence transport under wave forcing, alignment of the stress and Stokes drift impacts shear production (e.g. Fig. 2g). In realistic ocean conditions, winds and waves are often misaligned, reducing the component of momentum flux aligned with Stokes shear and thus lowering shear production relative to idealized aligned cases (Van Roekel et al. 2012). The L19 parameterization accounts for this effect by explicitly incorporating wind–wave misalignment through an integrated Stokes parameter, further improving the agreement between the parameterized shear production with LES shear production (Fig. 3b).

Overall, the L19 shear production parameterization accurately models the LES shear production (Fig. 3b), so the underestimation of dissipation by the L19 parameterization in (Fig. 3d) is not due to a failure to capture the shear production. Conversely, the wall and slab shear production parameterizations significantly overestimate the LES shear production even at 0.05 and $0.1h$ in (Fig. 3b), so their relatively accurate estimate of dissipation is not due to their accurate modeling of shear production under Stokes forcing.

This realistically-forced LES corroborates previous studies showing that shear production does not locally balance dissipation under Stokes forcing (Fig. 3d), highlighting the role of turbulent transport, even in the surface layer.

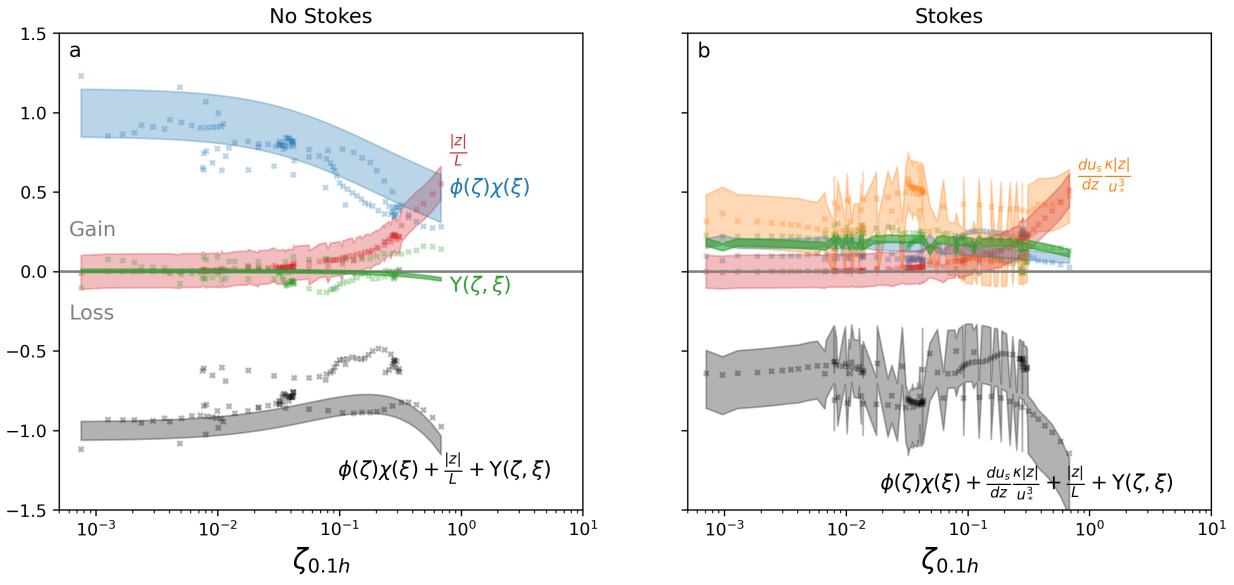

FIG. 4. Non-dimensional TKE budget at $0.1h$ during the same time period as in Fig. 3. a) No Stokes, b) Stokes forcing. Positive values represent turbulence production and negative values represent turbulence loss. Markers show data points from the LES. Shading shows the range of predictions from similarity functions (also annotated). Red: Buoyancy Production, Blue: Eulerian Shear Production, Orange: Stokes Shear Production, Green: Turbulence transport, Black: Turbulence dissipation rate.

c. Dependence of transport on the stability parameter

Since dissipation, a measurement of the rate of conversion of turbulence to heat, is the primary measure of turbulent mixing in the ocean, it is useful to understand the relationship between dissipation and the TKE budget. Wyngaard and Coté (1970) find an imbalance between measured terms of the TKE budget under very unstable conditions (strong convective cells) in the atmosphere that they attribute to turbulent transport. Similarly here, but instead for the case of Langmuir cells, we assess the LES terms of the TKE budget. We use this to build a quantitative model of the transport of TKE by considering the non-dimensional terms of the TKE budget and their associated similarity functions as a function of the stability parameter, ζ at $0.1h$ for No Stokes and Stokes cases (Fig. 4). Under neutral conditions ($|\zeta| \leq 10^{-1}$) in the No Stokes case (Fig. 4a), shear production balances dissipation, while buoyancy production and turbulence transport are negligible. For the same conditions under Stokes forcing (Fig. 4b), Eulerian shear production

is reduced to $\sim$ 20% of its No Stokes value, with the largest contribution to shear production derived from Stokes Shear (orange in Fig. 4b). The transport term is no longer negligible, with an almost equivalent contribution to the balance of turbulence dissipation as that of Eulerian shear production.

Thus, under realistic neutral wind-wave forced conditions, dissipation is balanced by shear production and transport following the form of Eq. 15 (Fig. 4b), similarly to that observed in the atmosphere under strong convection (Wyngaard and Coté 1970), and as discussed in a number of studies focused on Langmuir Circulation (Polton and Belcher 2007; Gerbi et al. 2009; Grant and Belcher 2009; Jarosz et al. 2021).

Large et al. (2019a,b, 2021b) suggest that in the Southern Ocean under Stokes forcing, a similarity theory approach can be reasonably applied to model turbulent velocity scales - essentially treating Stokes drift as a surface forcing. We extend this reasoning to turbulent transport by fitting a simple multiple linear regression to non-dimensional LES TKE transport (scaled by $u_*^3/k|z|$) to derive the empirical function, $\Upsilon_m(\xi,\zeta)$ that is a function of the stability parameter and the Stokes parameter, shown in Fig. 5:

$$\mathrm{T_m}(\xi,\zeta) \approx \Upsilon_m(\xi,\zeta) = 0.00475 + 0.25\xi - 0.08\zeta, \tag{23}$$

This gives an empirically determined universal quantitative functional representation of dimensionless transport. The function defined by Eq. 23 explains 65% of the variance in transport at the base of the surface-layer in the LES which spans a wide parameter space (see Fig. A1). Nevertheless further LES studies are needed in different parameter spaces (e.g. stable/strongly convective) to more extensively test Eq. 23 and refine our understanding.

Finally, the non-dimensional law-of-the-wall scaling for dissipation is extended to unstable, wavey conditions:

$$\varepsilon\frac{\kappa|z|}{u_*^3} = \phi_m(\zeta)\chi_m(\xi) + \frac{dU_s}{dz}\frac{\kappa|z|}{u_*^3} + \frac{z}{L} + \Upsilon_m(\xi,\zeta) \tag{24}$$

With Eq. 24, we have now built on L19 to include turbulent transport giving a scaling for dissipation that is representative of surface boundary layer with wave contributions under weak or neutral buoyancy forcing. This provides a physically grounded interpretation of dissipation observations in regimes where Langmuir turbulence is significant.

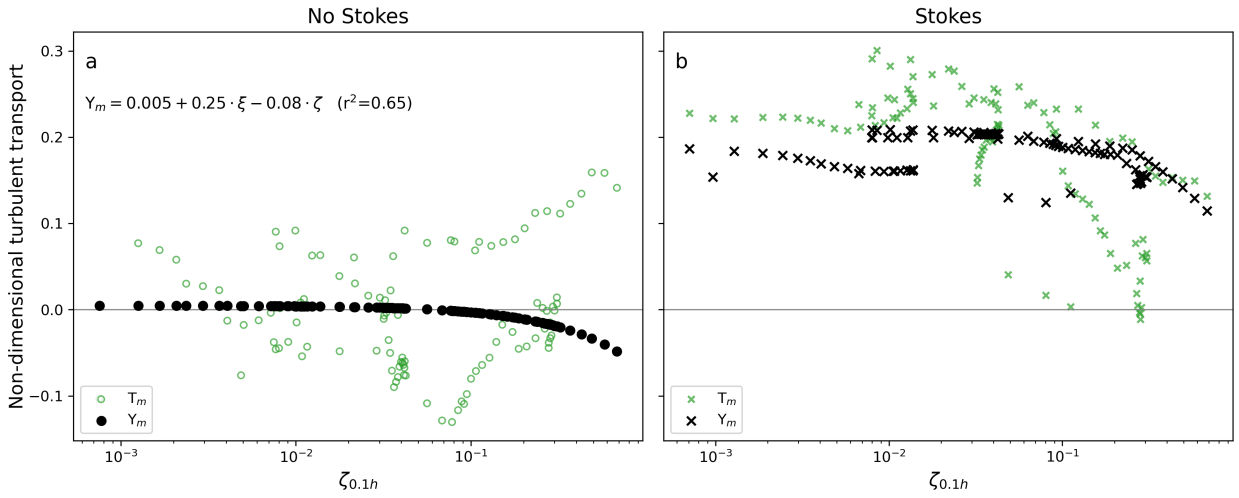

FIG. 5. Non-dimensional similarity functional fit, $\Upsilon_m(\xi, \zeta)$, (Eq. 23), of the convergence of turbulence transport of turbulence kinetic energy in terms of the Stokes parameter ξ and the stability parameter ζ, plotted along ζ at $0.1h$, derived from LES solutions during the same time periods as in Fig. 3. a) No Stokes b) Stokes. The green markers indicate the dimensionless convergence of TKE due to turbulent transport T_m, and the black markers show Υ_m. The fit from the combination of Stokes and No Stokes data has an r^2 of 0.65.

5. Scaling observations of dissipation in the Southern Ocean

The four (wall-scaling, slab wall-scaling, L19 and L19+transport) semi-empirical similarity functions for dissipation in the surface layer are now compared to observations of dissipation in the SAZ, APZ and SIZ during destabilizing buoyancy conditions. Both the observed and similarity-derived profiles are vertically-averaged from 5 to 15 m. This depth average ranges between 0.1-0.5h depending on the depth of h (Fig. B1). Averaging from 5 m is a necessity due to limitations in the data as noted in section 3b (limited data in upper 5-10 m). A lower bound of 15 m is chosen as a compromise providing sufficient data and reasonable results. The 5-15 m depth range is also easily observable and thus a useful metric for microstructure observations in the ocean. Following the vertical averaging, a profile-wise rolling mean of 4 profiles (and about 16 hours) is applied, thereby averaging over the inertial periods in these regions.

First consider predictions of observed dissipation assuming wind-driven shear production only. Law-of-the-wall (Eq. 6) explains 75-85% of the variance in all regions, with a tendency to over-estimate dissipation rates (Fig. 6a-c). This overestimation is most exaggerated in the SAZ and

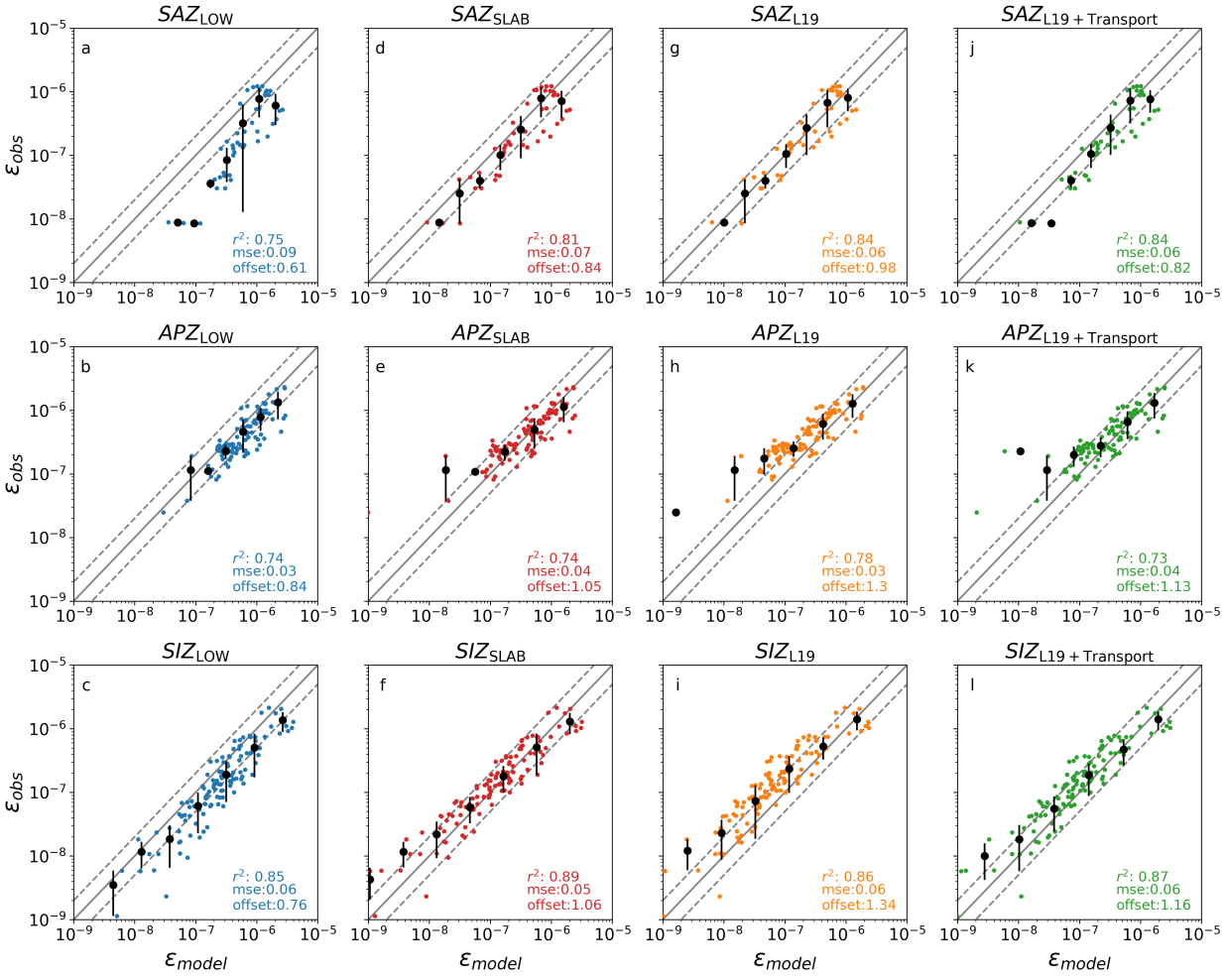

FIG. 6. Models for turbulence dissipation compared to observations of turbulence dissipation in three Southern Ocean locations during destabilizing buoyancy conditions. Top panel: the Subantarctic Zone (SAZ); middle panel: the Antarctic Polar Frontal Zone (APZ) and bottom panel: the Seasonal Ice Zone (SIZ). (a-c) Law-of-the-wall, Eq. 6, (d-f) Slab, Eq. 8, (g-i) Large et al 2019, Eq. 13 and (j-l) Large et al 2019 plus transport (Eq. 24), with transport defined in this manuscript (Eq. 23). The solid grey line indicates a 1:1 agreement. The dashed grey lines show a factor of 2 offset from the 1:1 line. Black markers indicate binned averages, with the errorbars showing the interquartile range. The r-square value, mean-square error and bias from the mean of the regressions are indicated in the legends of each panel.

during weaker forcing (lower values of dissipation rate). During the observational campaign, the SAZ experienced the shallowest boundary layers, such that an average of 5-15 m is well below $0.1h$, invalidating the assumption of constant momentum flux. Adjusting for a linearly decaying

momentum flux (Eq. 8) improves the variance explained and removes the bias averaged across all regions (Fig. 6d-f).

Now consider predictions of observed dissipation accounting for wind and wave driven shear production. L19 (Eq. 13) explains ~80% of the variance across all regions, where shear production is now largely attributed to Stokes drift as opposed to friction velocity, but the parameterization tends to underestimate observed dissipation rates (Fig. 6g-i). Adjusting L19 for the redistribution of turbulence via the transport of TKE (Eq. 24) reduces this bias by ~20% (Fig. 6j-l).

An outstanding observation is that the law-of-the-wall slab scaling and the modified L19+Transport-slab scaling can explain the variability and magnitude of observed dissipation rates equally well even though they represent different physics. The wall scaling (and the wall slab-scaling) represents a shear resulting from wind stress, while the modified L19+Transport-slab scaling represents a shear from Stokes drift, a shear from wind stress, a buoyancy flux (and the interactions of Stokes drift and buoyancy on the Eulerian shear) as well as a turbulent transport term. With Eq. 24 we have therefore provided a new quantitative parameterization of the TKE budget that includes all the terms of the TKE budget and reproduces both realistically-forced LES over a broad parameter space (Fig. 4) and observations in the Southern Ocean (Fig. 6).

6. Discussion and conclusions

Through the interrogation of realistically-forced LES across a wide parameter space of wind and wave forcing we have developed a similarity scaling for the dissipation of TKE (Eq. 24) that is a more physically consistent representation of dissipation under the wave-forced conditions that dominate in the Southern Ocean. Specifically this scaling, based on similarity theory, builds on the scaling of Large et al. (2019a) to include all four terms of the TKE budget: Eulerian shear production, Stokes shear production, Buoyancy production and turbulent transport. We find that turbulent transport can be represented in a non-dimensional functional form (Eq. 23) with a dependence on buoyancy flux and Stokes drift and incorporated within a similarity scaling framework (Eq. 24). This scaling is representative to both realistically-forced LES where the full TKE budget is explicitly simulated (Large et al. 2021a) and a suite of observations in the Southern Ocean (Giddy et al. 2025), where dissipation rates are measured directly. We expect that it will be applicable to cases at least within the parameter space tested here (weak buoyancy forcing, wind-wave forcing mostly in equilibrium).

Further work is needed to assess if the parameterizations used and developed here are applicable in other parts of parameter space.

Idealized LES studies that incorporate the surface wave effects encapsulated the wave-averaged Craik-Leibovich (CL) equations and compare dissipation profiles with wall scaling have shown that dissipation is enhanced relative to wall-scaling predictions (e.g. McWilliams et al. 1997; Grant and Belcher 2009). Realistically-forced LES that solve for the CL vortex force (include wave effects) more closely match dissipation observations (e.g. Skyllingstad et al. 2023; Pham et al. 2023), but their results have not been directly compared to wall-scaling - a common metric used to analyze observations of dissipation. Exceptions (reduced dissipation to that expected) have been noted that arise when winds and waves are misaligned (e.g. Van Roekel et al. 2012) and when swell is important (e.g. Fan et al. 2020). In this study, we compare realistically-forced LES with and without Stokes forcing and observed dissipation profiles with law-of-the-wall. Law-of-the-wall is found to be an accurate predictor of surface-layer dissipation in the Southern Ocean (Fig. 3c,d; Fig. 6a-c). This is consistent with a number of prior observational studies (e.g. Gerbi et al. 2009; Sutherland et al. 2013; Esters et al. 2018; Ferris et al. 2022; Miller et al. 2023; Zeiden et al. 2024). The slab wall-scaling improves the fit as many of our observations are taken below the surface-layer. It is intriguing that the physics-aligned scaling we present (Eq. 24) does not perform statistically better against our observations than the slab wall-scaling that does not account for wave physics. In part, the similarity across parameterizations may be reflecting the approximately linear relation between Stokes drift and friction velocity (e.g. Esters et al. 2018; Gargett 2022). This result may appear to suggest that surface gravity waves and Stokes drift are not participating in the TKE budget and specifically the dissipation rate in the surface-layer. Zippel et al. (2022) follow this hypothesis with data from the North Atlantic, splitting the boundary layer into a breaking wave layer (upper few meters) in which turbulence is enhanced from breaking waves and the layer below down to the base of the boundary layer, which is explained by the slab wall-scaling. However, since our scaling, which includes transport and Stokes shear production, performs equally well as the slab-scaling, we cannot corroborate their results with the same physical argument. While in the regimes sampled in this study and for example that of Zippel et al. (2022), the wall-scaling well represents dissipation, we have shown here with realistically-forced LES that the physics behind the wall-scaling is not representative of the actual physics at play. As such we cannot be certain that

the law-of-the-wall will hold in all regime spaces. And indeed, deviations from the wall-scaling compared to dissipation measurements when waves are present is often observed, supporting our interpretation (D'Asaro et al. 2014; Sutherland et al. 2016; Jarosz et al. 2021; Zheng et al. 2021).

In all parameterizations and across all the regions observed there is a remaining variance of ~20%. Part of this variability may reflect the natural intermittency of turbulence (e.g., Moum et al. 1995). Remaining variance in dissipation may be attributed to limitations in using reanalysis wind and modeled waves, inadequate representation of stress-shear misalignment, unaccounted for sources of shear production or imperfect closure of the TKE budget. In addition to Langmuir turbulence, other boundary layer processes can modify both the Langmuir turbulence directly as well as acting as additional sources or sinks of turbulence dissipation. The transport of TKE is non-negligible for the local TKE balance under cases of strong convection as shown in the atmosphere (e.g. Wyngaard and Coté 1970). Time-varying wind (e.g. Watkins and Whitt 2020) and wave (e.g. Wagner et al. 2021) forcing can excite the growth of near-inertial waves which act as a source of shear and the rate of growth of the waves modulates Langmuir turbulence (Wagner et al. 2021). In the simulated dissipation of the LES presented here, near-inertial resonance likely contributes to enhanced shear at the base of the boundary layer in both wind and wind-wave forced cases, illustrated in Fig. 2b,f. The effects of differences in the rate of growth of waves has not been explored. The presence of fine-scale lateral fronts will also modify turbulence. Submesoscale mixed layer eddies are associated with overturning cells with strong vertical velocities (Fox-Kemper et al. 2008). Winds aligned with fronts provide energy to maintain the geostrophic shear, and thus turbulence, associated with those fronts (Thomas et al. 2016). In this study, lateral processes are not resolved in the simulation and while they may be present in the observations, they do not appear to play a dominant role – at least in the upper half of the boundary layer since the wind forcing is much greater than the strength of the lateral gradients ($O(10^{-8})$). The small contribution of submesoscale instabilities to the TKE budget was shown in observations by (Buckingham et al. 2019), however they may become important in other regimes (Dong et al. 2024). Since the parameterizations tested here perform similarly across the three regions of our observations (Fig. 6), we speculate that turbulence related to submesoscale fronts (D'Asaro et al. 2011; Thomas et al. 2016; Yu et al. 2019; Dong et al. 2024), and the effects of time-varying processes like inertial oscillations which would be expected to vary with latitude (Large and Crawford 1995; Dohan and Davis 2011; Watkins and Whitt 2020)

are secondary sources of shear production in the surface layer, and likely only play a substantial role in the outer boundary layer – at deeper depths than the focus of this analysis, but important to consider if closing the full boundary layer budget with this framework. A focus on these processes, especially their role in the TKE budget in the outer boundary layer in the Southern Ocean is left to future work.

A weakness of the observational data is that we largely miss the upper 5 m, where Stokes shear production is expected to be its strongest as Stokes drift follows an exponential decay. Because of the limited near-surface observations we also did not consider the role of breaking waves (e.g. Agrawal et al. 1992; Zippel et al. 2022), although we do not expect the results here to be sensitive to breaking waves because their impact is generally confined to one significant wave height (approximately 8 m at its maximum in the conditions of these observations). In addition, lacking co-located observations of forcing variables we relied on model and reanalysis products in this study, which could add further uncertainty. Nevertheless, the results are consistent with the proposed physics based on realistically-forced LES of the Southern Ocean, giving confidence to the conclusions drawn here. The conclusions of this analysis apply to the upper ocean surface boundary layer, under moderate to strong wind and wave forcing, weak stratification and weak destabilizing buoyancy forcing. Cases of strongly stabilizing buoyancy, weak and variable winds, rapidly changing winds and strong convection were not considered. LES over a broader range of conditions representative of the real ocean together with observations would enable further generalization of these conclusions. Future observational studies could reduce uncertainty through co-located observations of surface forcing, direct observation of friction velocity (e.g. with a sonic anemometer), and measurements of Stokes and Eulerian shear in conjunction with turbulence dissipation.

Acknowledgments. IG is supported by the Swedish Research Council International Postdoctoral Fellowship (VR 2022-00395) and Wallenberg Academy Fellowship of SS (WAF 2015.0186). ØB and IF gratefully acknowledge the support of the Research Council of Norway (RCN) through the ENTIRE project (grant no 324227) and the KeyPOCP project (grant no 328941), respectively. DW was supported by the NASA Earth Science research and analysis and Earth Action programs, including grants 80NSSC20K0890 and 80NSSC19K1116. SS has received funding from the European Union's Horizon Europe ERC Synergy Grant programme under grant agreement No. 101118693 (WHIRLS), and the Swedish Research Council (VR 2019-04400). SN acknowledges support from three consecutive NRF-SANAP grants (SNA170522231782,SANAP200324510487,SANAP230503101416), which have made the collection of in-situ glider dissipation observations possible. We acknowledge and thank Bill Large for publishing his LES solutions and making them easy to use as well as for some insightful discussions early in the project. We thank those part of the collective effort in deploying and piloting the gliders, in particular Sea Technology Services and the officers and crew of the RV SA Agulhas II. IG gratefully acknowledges and thanks Susan Alexander and ARC-CREST for facilitating her research visit to NASA Ames/CSUMB. We thank three anonymous reviewers for their comments which have improved this manuscript.

Data availability statement. Large Eddy Simulations are made available by Large et al (2021) at https://doi.org/10.5065/87n8-9r86. The in situ data glider and microstructure data is available via Zenodo (Giddy et al. 2025) at https://doi.org/10.5281/zenodo.14981745. ECMWF Reanalysis, ERA5, (Hersbach et al. 2023) was downloaded from the Copernicus Climate Change Service (2024). The Antarctic Circumpolar Current (ACC) - fronts product used in Fig. 1, DOI: 10.24400/527896/a01-2023.004, was produced by CTOH and distributed by AVISO+ (https://www.aviso.altimetry.fr/) with support from CNES.

APPENDIX A

LES Forcing and Surface Current Response

Fig A1 describes the surface forcing imposed on the LES for April and June cases. Note the predominantly convective conditions in Fig A1c. Fig A1d illustrates the Eulerian surface currents under the No Stokes cases while Fig A1e illustrates the Eulerian surface currents under the Stokes cases. Oscillations spanning 15 hours (about the inertial period at this latitude, 42^o S) indicate the presence of inertial oscillations in all cases. These are most prominent in April (solid lines). Under the Stokes forcing cases the mean Eulerian current is reduced in magnitude, but the oscillations remain.

APPENDIX B

Observations in the Southern Ocean

a. Dissipation

Fig. B1 details the dissipation sections from the Subantarctic Zone, the Antarctic Polar Frontal Zone and the Seasonal Ice Zone, computed from microstructure shear profiles as described in Section 3c, together with co-located surface forcing from ERA5 reanalysis.

b. In situ observations of wind speed compared to ERA5 reanalysis

During two of the Slocum glider deployments, part of the deployments were coupled to surface Wavegliders which were recording wind speed from and Airmar sensor mounted at a height of 1 m. Because the deployment were not coupled for the full missions we use ERA5 Reanalysis in this study, however here we show that using ERA5 reasonably captures the variance and magnitude of winds (which impose stress on the surface ocean and drive waves and mixing). The regressions of ERA5 with the in situ wind observations in Fig. B2b and B2c show that 80% of the variance observed is captured with ERA5, with ERA5 being biased low, especially at stronger wind speeds. Spectra of wind speeds from ERA5 and the Airmar observations are computed using a multi-taper spectral method with a smoothing of P=16, the time-bandwidth product. The resulting power density spectra (Fig. B2c and B2f) indicates that the energy containing scales (lower frequencies) of the winds are well represented in ERA5.

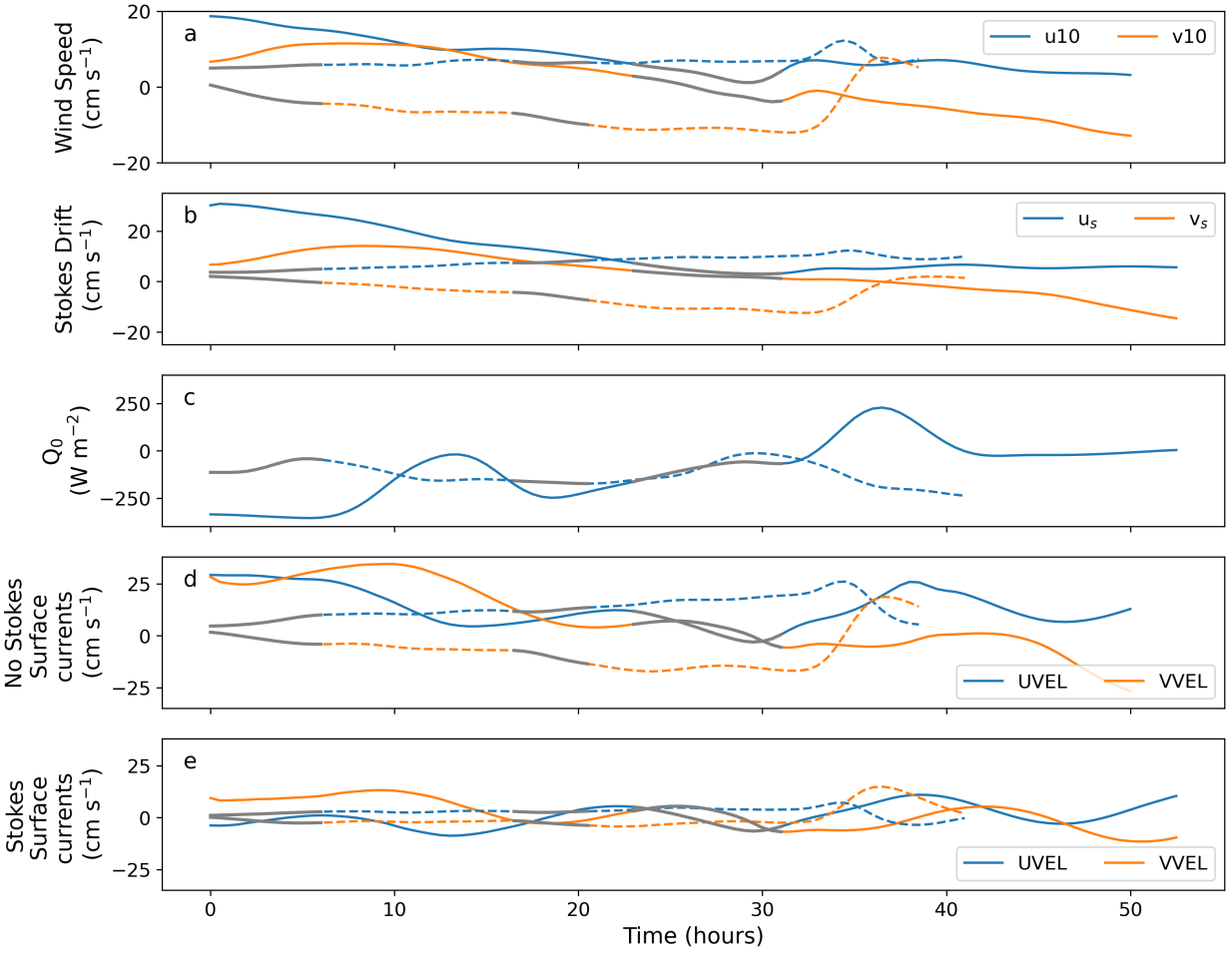

728 FIG. A1. Surface forcing in April (solid lines) and June (dashed lines) LES: a) Wind speed, b) Stokes Drift,
729 c) Surface heat flux, Q_0, and the Eulerian surface current response: d) No Stokes surface currents and e) Stokes
730 surface currents. Grey lines mark the regimes which are not included in this analysis.

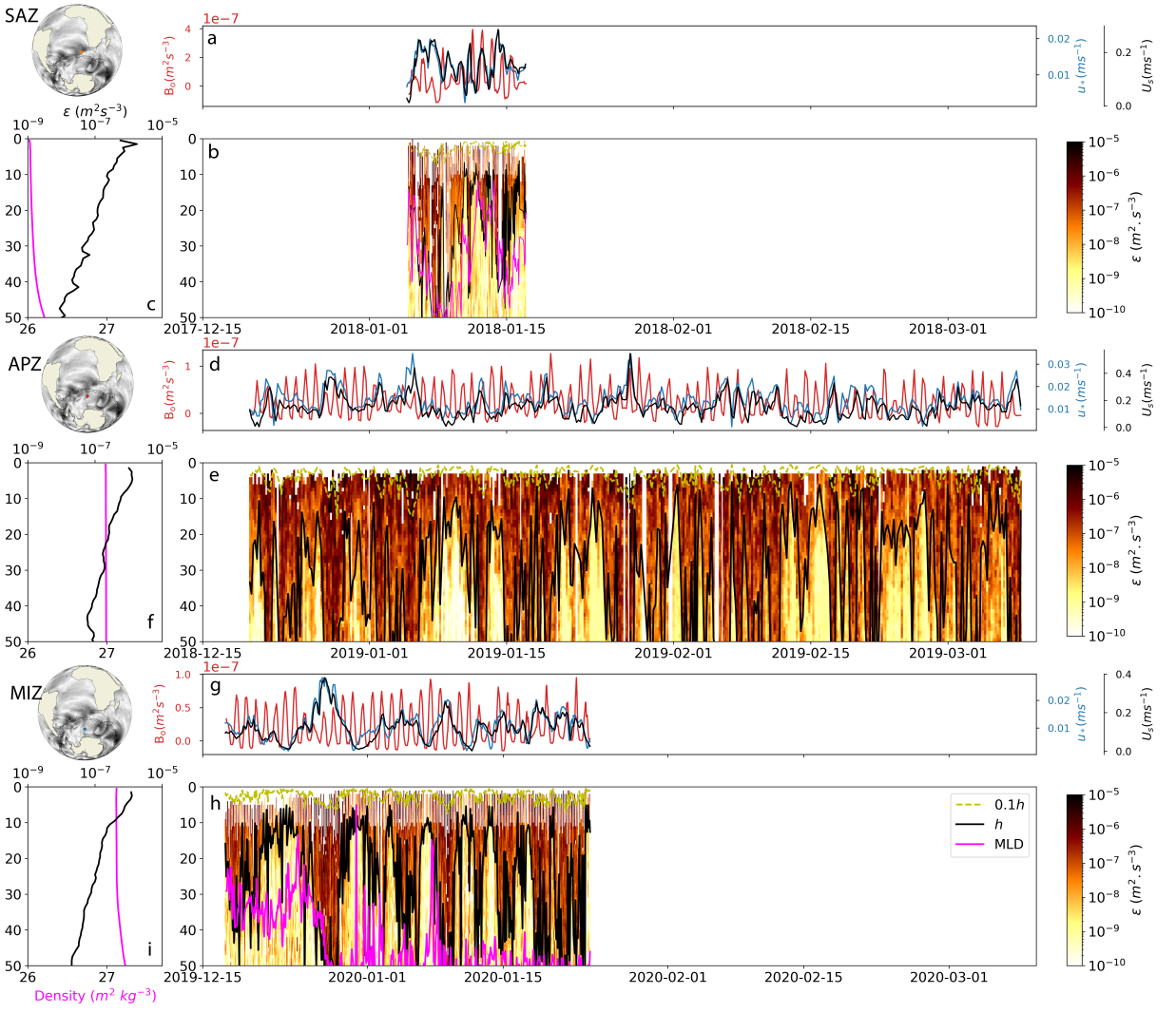

737 FIG. B1. Observed turbulence dissipation rate and their atmospheric forcing. a-c) the Subantarctic Zone,
738 2017-2018: a) Forcing, b) dissipation sections, c) mean profiles of density (magenta) and dissipation (black);
739 d-e) the Antarctic Polar Frontal Zone, 2018-2019: d) Forcing, e) dissipation section, f) mean profiles of density
740 (magenta) and dissipation (black); g-i) the Seasonal Ice Zone, 2019-2020: g) Forcing, h) dissipation section, i)
741 mean profiles of density (magenta) and dissipation (black). 0.1h (yellow dashed), h (solid black) and the mixed
742 layer depth (MLD) (solid magenta) are overlain in (b),(e) and (h). Each deployment occurred in a different year
743 but timeseries are aligned from December - March. The maps identify the locations of the deployments.

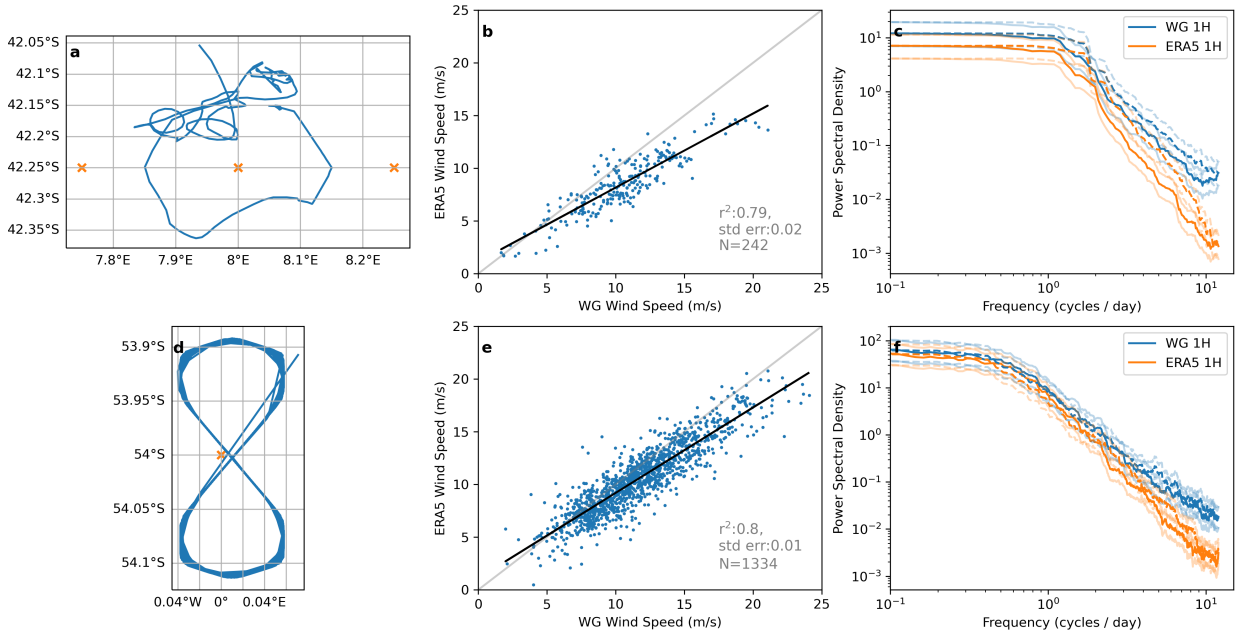

FIG. B2. Comparison of in situ wind observations from times when a Waveglider was couples with the Slocum during the deployments in the Subantarctic Zone (top row) and the Antarctic Polar Frontal Zone (lower row). Waveglider observations are interpolated to hourly from 10 minute samples. a,d) trajectories of the Wavegliders in blue, ERA5 in orange; b,e) Regressions of Waveglider observed wind speeds at 1 m adjusted to 10 m against co-located ERA5 reanalysis 10 m wind speeds, the grey line indicates a 1:1 agreement; c,f) Rotary spectra of wind speeds: Waveglider observations in blue, ERA5 reanalysis in orange, solid lines are the negative spectra, dashed lines are the positive spectra. 95% confidence intervals are shown.

References

Agrawal, Y. C., E. A. Terray, M. A. Donelan, P. A. Hwang, A. J. Williams, W. M. Drennan, K. K. Kahma, and S. A. Krtaigorodskii, 1992: Enhanced dissipation of kinetic energy beneath surface waves. *Nature*, **359 (6392)**, 219–220, https://doi.org/10.1038/359219a0.

Belcher, S. E., and Coauthors, 2012: A global perspective on Langmuir turbulence in the ocean surface boundary layer. *Geophysical Research Letters*, **39 (18)**, 2012GL052 932, https://doi.org/10.1029/2012GL052932.

Brainerd, K., and M. Gregg, 1995: Surface mixed and mixing layer depths. *Deep Sea Research Part I: Oceanography Research Papers*, **42 (9)**, 1521–1532.

Breivik, O., P. A. E. M. Janssen, and J.-R. Bidlot, 2014: Approximate Stokes Drift Profiles in Deep Water. *Journal of Physical Oceanography*, **44 (9)**, 2433–2445, https://doi.org/10.1175/JPO-D-14-0020.1.

Buckingham, C. E., N. S. Lucas, S. E. Belcher, T. P. Rippeth, A. L. M. Grant, J. Le Sommer, A. O. Ajayi, and A. C. Naveira Garabato, 2019: The Contribution of Surface and Submesoscale Processes to Turbulence in the Open Ocean Surface Boundary Layer. *Journal of Advances in Modeling Earth Systems*, **11 (12)**, 4066–4094, https://doi.org/10.1029/2019MS001801.

Businger, J., J. Wyngaard, Y. Izumi, and E. Bradley, 1971: Flux-Profile relationships in the atmospheric surface later. *Journal of Atmospheric Sciences*, **28**, 181–189.

Chen, B., D. Yang, C. Meneveau, and M. Chamecki, 2016: Effects of swell on transport and dispersion of oil plumes within the ocean mixed layer. *Journal of Geophysical Research: Oceans*, **121 (5)**, 3564–3578, https://doi.org/10.1002/2015JC011380.

Chor, T., J. C. McWilliams, and M. Chamecki, 2021: Modifications to the K-Profile Parameterization with Nondiffusive Fluxes for Langmuir Turbulence. *Journal of Physical Oceanography*, **51 (5)**, 1503–1521, https://doi.org/10.1175/JPO-D-20-0250.1.

Cifuentes-Lorenzen, A., C. J. Zappa, J. B. Edson, J. O'Donnell, and D. S. Ullman, 2024: Exploring the Role of Wave-Driven Turbulence at the Air-Sea Interface Through Measurements of TKE Dissipation Rates Across the Air-Sea Interface. *Journal of Geophysical Research: Oceans*, **129 (8)**, e2023JC020 308, https://doi.org/10.1029/2023JC020308.

Craik, A. D. D., and S. Leibovich, 1976: A rational model for Langmuir circulations. *Journal of Fluid Mechanics*, **73 (3)**, 401–426, https://doi.org/10.1017/S0022112076001420.

D'Asaro, E. A., J. Thomson, A. Y. Shcherbina, R. R. Harcourt, M. F. Cronin, M. A. Hemer, and B. Fox-Kemper, 2014: Quantifying upper ocean turbulence driven by surface waves. *Geophysical Research Letters*, **41 (1)**, 102–107, https://doi.org/10.1002/2013GL058193.

Dohan, K., and R. E. Davis, 2011: Mixing in the Transition Layer during Two Storm Events. *Journal of Physical Oceanography*, **41 (1)**, 42–66, https://doi.org/10.1175/2010JPO4253.1.

Dong, J., B. Fox-Kemper, J. O. Wenegrat, A. S. Bodner, X. Yu, S. Belcher, and C. Dong, 2024: Submesoscales are a significant turbulence source in global ocean surface boundary layer. *Nature Communications*, **15 (1)**, 9566, https://doi.org/10.1038/s41467-024-53959-y.

Du Plessis, M. D., S. Swart, L. C. Biddle, I. S. Giddy, P. M. S. Monteiro, C. J. C. Reason, A. F. Thompson, and S. Nicholson, 2022: The Daily-Resolved Southern Ocean Mixed Layer: Regional Contrasts Assessed Using Glider Observations. *Journal of Geophysical Research: Oceans*, **127 (4)**, e2021JC017 760, https://doi.org/10.1029/2021JC017760.

D'Asaro, E., C. Lee, L. Rainville, R. Harcourt, and L. Thomas, 2011: Enhanced Turbulence and Energy Dissipation at Ocean Fronts. *Science*, **332 (6027)**, 318–322, https://doi.org/10.1126/science.1201515.

ECMWF, 2013: IFS Documentation CY40r1, Part VII: ECMWF Wave model. ECMWF Model Documentation. European Centre for Medium-Range Weather Forecasts.

Esters, L., O. Breivik, S. Landwehr, A. Ten Doeschate, G. Sutherland, K. H. Christensen, J. Bidlot, and B. Ward, 2018: Turbulence Scaling Comparisons in the Ocean Surface Boundary Layer. *Journal of Geophysical Research: Oceans*, **123 (3)**, 2172–2191, https://doi.org/10.1002/2017JC013525.

Fairall, C. W., E. F. Bradley, J. E. Hare, A. A. Grachev, and J. B. Edson, 2003: Bulk Parameterization of Air–Sea Fluxes: Updates and Verification for the COARE Algorithm. *Journal of Climate*, **16 (4)**, 571–591, https://doi.org/10.1175/1520-0442(2003)016⟨0571:BPOASF⟩2.0.CO;2.

Fan, Y., and Coauthors, 2020: The effect of Langmuir turbulence under complex real oceanic and meteorological forcing. *Ocean Modelling*, **149**, 101 601, https://doi.org/10.1016/j.ocemod.2020.101601.

Fer, I., A. K. Peterson, and J. E. Ullgren, 2014: Microstructure Measurements from an Underwater Glider in the Turbulent Faroe Bank Channel Overflow. *Journal of Atmospheric and Oceanic Technology*, **31 (5)**, 1128–1150, https://doi.org/10.1175/JTECH-D-13-00221.1.

Ferris, L., D. Gong, C. A. Clayson, S. Merrifield, E. L. Shroyer, M. Smith, and L. S. Laurent, 2022: Shear Turbulence in the High-Wind Southern Ocean Using Direct Measurements. *Journal of Physical Oceanography*, **52 (10)**, 2325–2341, https://doi.org/10.1175/JPO-D-21-0015.1.

Foken, T., 2006: 50 Years of the Monin–Obukhov Similarity Theory. *Boundary-Layer Meteorology*, **119 (3)**, 431–447, https://doi.org/10.1007/s10546-006-9048-6.

Fox-Kemper, B., R. Ferrari, and R. Hallberg, 2008: Parameterization of Mixed Layer Eddies. Part I: Theory and Diagnosis. *Journal of Physical Oceanography*, **38 (6)**, 1145–1165, https://doi.org/10.1175/2007jpo3792.1.

Gargett, A. E., 2022: Forcing Space: An Alternative to Regime Diagrams for Predicting Characteristics of Turbulence in the Ocean Surface Mixing Layer. *Journal of Physical Oceanography*, **52 (3)**, 519–535, https://doi.org/10.1175/JPO-D-21-0145.1.

Gerbi, G. P., J. H. Trowbridge, E. A. Terray, A. J. Plueddemann, and T. Kukulka, 2009: Observations of Turbulence in the Ocean Surface Boundary Layer: Energetics and Transport. *Journal of Physical Oceanography*, **39 (5)**, 1077–1096, https://doi.org/10.1175/2008JPO4044.1.

Giddy, I., I. Fer, and S.-A. Nicholson, 2025: Dissipation measurements from a Slocum Glider in Southern Ocean during austral summer 2017, 2018 and 2019. Zenodo, https://doi.org/10.5281/zenodo.14981745.

Giddy, I. S., I. Fer, S. Swart, and S.-A. Nicholson, 2023: Vertical Convergence of Turbulent and Double-Diffusive Heat Flux Drives Warming and Erosion of Antarctic Winter Water in Summer. *Journal of Physical Oceanography*, **53 (8)**, 1941–1958, https://doi.org/10.1175/JPO-D-22-0259.1.

Grant, A. L. M., and S. E. Belcher, 2009: Characteristics of Langmuir Turbulence in the Ocean Mixed Layer. *Journal of Physical Oceanography*, **39 (8)**, 1871–1887, https://doi.org/10.1175/2009JPO4119.1.

Gruber, N., P. Landschützer, and N. S. Lovenduski, 2019: The Variable Southern Ocean Carbon Sink. *Annual Review of Marine Science*, **11 (1)**, 159–186, https://doi.org/10.1146/annurev-marine-121916-063407.

Harcourt, R. R., and E. A. D'Asaro, 2008: Large-Eddy Simulation of Langmuir Turbulence in Pure Wind Seas. *Journal of Physical Oceanography*, **38 (7)**, 1542–1562, https://doi.org/10.1175/2007JPO3842.1.

Hersbach, H., and Coauthors, 2020: The ERA5 global reanalysis. *Quarterly Journal of the Royal Meteorological Society*, **146 (730)**, 1999–2049, https://doi.org/10.1002/qj.3803.

Hersbach, H., and Coauthors, 2023: ERA5 hourly data on pressure levels from 1940 to present. Copernicus Climate Change Service (C3S) Climate Data Store (CDS), https://doi.org/10.24381/cds.bd0915c6.

Hogstrom, U., 1988: Non-dimensional wind and temperature profiles in the atmospheric surface layer: A re-evaluation. *Boundary-Layer Meteorology*, **42**, 55–78.

Jarosz, E., H. W. Wijesekera, and D. W. Wang, 2021: Coherent Velocity Structures in the Mixed Layer: Characteristics, Energetics, and Turbulent Kinetic Energy Budget. *Journal of Physical Oceanography*, **51 (9)**, 2991–3014, https://doi.org/10.1175/JPO-D-20-0248.1.

Kenyon, K. E., 1969: Stokes drift for random gravity waves. *Journal of Geophysical Research*, **74 (28)**, 6991–6994, https://doi.org/10.1029/JC074i028p06991.

Kukulka, T., A. J. Plueddemann, and P. P. Sullivan, 2012: Nonlocal transport due to Langmuir circulation in a coastal ocean. *Journal of Geophysical Research: Oceans*, **117 (C12)**, 2012JC008 340, https://doi.org/10.1029/2012JC008340.

Kukulka, T., A. J. Plueddemann, J. H. Trowbridge, and P. P. Sullivan, 2009: Significance of Langmuir circulation in upper ocean mixing: Comparison of observations and simulations. *Geophysical Research Letters*, **36 (10)**, 2009GL037 620, https://doi.org/10.1029/2009GL037620.

Large, B., E. Patton, A. DuVivier, and P. Sullivan, 2021a: Large Eddy Simulation of the Southern Ocean. *UCAR/NCAR - GDEX*, https://doi.org/https://doi.org/10.5065/87n8-9r86.

Large, W., and G. Crawford, 1995: Observations and simulations of upper ocean response to wind events during the Ocean Storms experiment. *Journal of Physical Oceanography*, **25**, 2831–2852.

Large, W. G., J. C. McWilliams, and S. C. Doney, 1994: Oceanic vertical mixing: A review and a model with a nonlocal boundary layer parameterization. *Reviews of Geophysics*, **32 (4)**, 363–403, https://doi.org/10.1029/94RG01872.

Large, W. G., E. G. Patton, A. K. DuVivier, P. P. Sullivan, and L. Romero, 2019a: Similarity Theory in the Surface Layer of Large-Eddy Simulations of the Wind-, Wave-, and Buoyancy-Forced Southern Ocean. *Journal of Physical Oceanography*, **49 (8)**, 2165–2187, https://doi.org/10.1175/JPO-D-18-0066.1.

Large, W. G., E. G. Patton, and P. P. Sullivan, 2019b: Nonlocal Transport and Implied Viscosity and Diffusivity throughout the Boundary Layer in LES of the Southern Ocean with Surface Waves. *Journal of Physical Oceanography*, **49 (10)**, 2631–2652, https://doi.org/10.1175/JPO-D-18-0202.1.

Large, W. G., E. G. Patton, and P. P. Sullivan, 2021b: The Diurnal Cycle of Entrainment and Detrainment in LES of the Southern Ocean Driven by Observed Surface Fluxes and Waves. *Journal of Physical Oceanography*, **51 (10)**, 3253–3278, https://doi.org/10.1175/JPO-D-20-0308.1.

Leibovich, S., 1983: The form and dynamics of Langmuir Circulations. *Annual Review of Fluid Mechanics*, **15 (1)**, 391–427, https://doi.org/10.1146/annurev.fl.15.010183.002135.

Li, Q., and Coauthors, 2019: Comparing Ocean Surface Boundary Vertical Mixing Schemes Including Langmuir Turbulence. *Journal of Advances in Modeling Earth Systems*, **11 (11)**, 3545–3592, https://doi.org/10.1029/2019MS001810.

Liu, J., J.-H. Liang, J. C. McWilliams, P. P. Sullivan, Y. Fan, and Q. Chen, 2018: Effect of Planetary Rotation on Oceanic Surface Boundary Layer Turbulence. *Journal of Physical Oceanography*, **48 (9)**, 2057–2080, https://doi.org/10.1175/JPO-D-17-0150.1.

Lombardo, C. P., and M. C. Gregg, 1989: Similarity scaling of viscous and thermal dissipation in a convecting surface boundary layer. *Journal of Geophysical Research: Oceans*, **94 (C5)**, 6273–6284, https://doi.org/10.1029/JC094iC05p06273.

Lueck, R., and Coauthors, 2024: Best practices recommendations for estimating dissipation rates from shear probes. *Frontiers in Marine Science*, **11**, 1334 327, https://doi.org/10.3389/fmars.2024.1334327.

Marshall, J., J. R. Scott, and K. C. Armour, 2015: The ocean's role in the transient response of climate to abrupt greenhouse gas forcing. *Climate Dynamics*, **44**, 2287–2299.

McDougall, T., and P. Barker, 2011: Getting started with TEOS-10 and the Gibbs Seawater (GSW) Oceanographic Toolbox. *SCOR/IAPSO WG127*, 22.

McWilliams, J. C., and P. P. Sullivan, 2000: Vertical Mixing by Langmuir Circulations. *Spill Science & Technology Bulletin*, **6 (3-4)**, 225–237, https://doi.org/10.1016/S1353-2561(01)00041-X.

McWilliams, J. C., P. P. Sullivan, and C.-H. Moeng, 1997: Langmuir turbulence in the ocean. *Journal of Fluid Mechanics*, **334**, 1–30, https://doi.org/10.1017/S0022112096004375.

Miller, U. K., C. J. Zappa, S. F. Zippel, J. T. Farrar, and R. A. Weller, 2023: Scaling of Moored Surface Ocean Turbulence Measurements in the Southeast Pacific Ocean. *Journal of Geophysical Research: Oceans*, **128 (1)**, e2022JC018 901, https://doi.org/10.1029/2022JC018901.

Moeng, C.-H., 1984: A Large-Eddy-Simulation Model for the Study of PLanetary Boundary-Layer Turbulence. *Journal of Atmospheric Sciences*, **41 (13)**, 2052–2062.

Monin, A., and A. Obukhov, 1954: Basic laws of turbulent mixing in the surface layer of the atmosphere. *Contrib. Geophys. Inst. Acad. Sci. USSR*, **151 (163)**, e187.

Moum, J., M. Gregg, R. Lien, and M. Carr, 1995: Comparison of Turbulence Kinetic Energy Dissipation Rate Estimates from Two Ocean Microstructure Profilers. *Journal of Atmospheric and Oceanic Technology*, **12 (2)**, 346–366.

Nicholson, S.-A., D. B. Whitt, I. Fer, M. D. Du Plessis, A. D. Lebéhot, S. Swart, A. J. Sutton, and P. M. S. Monteiro, 2022: Storms drive outgassing of CO2 in the subpolar Southern Ocean. *Nature Communications*, **13 (1)**, 158, https://doi.org/10.1038/s41467-021-27780-w.

Noh, Y., G. Goh, and S. Raasch, 2011: Influence of Langmuir Circulation on the Deepening of the Wind-Mixed Layer. *Journal of Physical Oceanography*, **41 (3)**, 472–484, https://doi.org/10.1175/2010JPO4494.1.

Pham, H. T., S. Sarkar, L. Johnson, B. Fox-Kemper, P. P. Sullivan, and Q. Li, 2023: Multi-Scale Temporal Variability of Turbulent Mixing During a Monsoon Intra-Seasonal Oscillation in the Bay of Bengal: An LES Study. *Journal of Geophysical Research: Oceans*, **128 (1)**, e2022JC018 959, https://doi.org/10.1029/2022JC018959.

Polton, J. A., and S. E. Belcher, 2007: Langmuir turbulence and deeply penetrating jets in an unstratified mixed layer. *Journal of Geophysical Research: Oceans*, **112 (C9)**, 2007JC004 205, https://doi.org/10.1029/2007JC004205.

Sallée, J. B., K. Speer, and R. Morrow, 2008: Response of the Antarctic Circumpolar Current to Atmospheric Variability. *Journal of Climate*, **21 (12)**, 3020–3039, https://doi.org/10.1175/2007JCLI1702.1.

Schulz, E. W., S. A. Josey, and R. Verein, 2012: First air-sea flux mooring measurements in the Southern Ocean. *Geophysical Research Letters*, **39 (16)**, 2012GL052 290, https://doi.org/10.1029/2012GL052290.

Skyllingstad, E. D., and D. W. Denbo, 1995: An ocean large-eddy simulation of Langmuir circulations and convection in the surface mixed layer. *Journal of Geophysical Research: Oceans*, **100 (C5)**, 8501–8522, https://doi.org/10.1029/94JC03202.

Skyllingstad, E. D., R. M. Samelson, H. Simmons, L. S. Laurent, S. Merrifield, T. Klenz, and L. Centurioni, 2023: Boundary Layer Energetics of Rapid Wind and Wave Forced Mixing Events. *Journal of Physical Oceanography*, **53 (8)**, 1887–1900, https://doi.org/10.1175/JPO-D-22-0150.1.

Smith, J. A., 1992: Observed growth of Langmuir circulation. *Journal of Geophysical Research: Oceans*, **97 (C4)**, 5651–5664, https://doi.org/10.1029/91JC03118.

Smyth, W. D., E. D. Skyllingstad, G. B. Crawford, and H. Wijesekera, 2002: Nonlocal fluxes and Stokes drift effects in the K-profile parameterization. *Ocean Dynamics*, **52 (3)**, 104–115, https://doi.org/10.1007/s10236-002-0012-9.

Stull, R. B., 1988: Similarity Theory. *An Introduction to Boundary Layer Meteorology*, R. B. Stull, Ed., Springer Netherlands, Dordrecht, 347–404, https://doi.org/10.1007/978-94-009-3027-8_9, URL https://doi.org/10.1007/978-94-009-3027-8_9.

Sullivan, P. P., J. C. McWilliams, and C.-H. Moeng, 1994: A subgrid-scale model for large-eddy simulation of planetary boundary-layer flows. *Boundary-Layer Meteorology*, **71 (3)**, 247–276, https://doi.org/10.1007/BF00713741.

Sutherland, G., K. H. Christensen, and B. Ward, 2014: Evaluating Langmuir turbulence parameterizations in the ocean surface boundary layer. *Journal of Geophysical Research: Oceans*, **119 (3)**, 1899–1910, https://doi.org/10.1002/2013JC009537.

Sutherland, G., L. Marié, G. Reverdin, K. H. Christensen, G. Broström, and B. Ward, 2016: Enhanced Turbulence Associated with the Diurnal Jet in the Ocean Surface Boundary Layer. *Journal of Physical Oceanography*, **46 (10)**, 3051–3067, https://doi.org/10.1175/JPO-D-15-0172.1.

Sutherland, G., B. Ward, and K. H. Christensen, 2013: Wave-turbulence scaling in the ocean mixed layer. *Ocean Science*, **9 (4)**, 597–608, https://doi.org/10.5194/os-9-597-2013.

Swain, J., P. Umesh, and A. Balchand, 2019: WAM and WAVEWATCH-III intercomparison studies in the North Indian Ocean using Oceansat-2 Scatterometer winds. *Journal of Ocean and Climate: Science, Technology and Impacts*, **9**, 2516019219866 569, https://doi.org/10.1177/2516019219866569.

Swart, S., and Coauthors, 2012: Southern Ocean Seasonal Cycle Experiment 2012: Seasonal scale climate and carbon cycle links. *South African Journal of Science*, **108 (3/4)**, 3 pages, https://doi.org/10.4102/sajs.v108i3/4.1089.

Terray, E., M. Donelan, Y. Agrawal, W. Drennan, K. Kahma, A. Williams III, P. Hwang, and S. Kitaigorodskii, 1996: Estimates of kinetic energy dissipation under breaking waves. *Journal of Physical Oceanography*, **26**, 792–807.

Thomas, L. N., J. R. Taylor, E. A. D'Asaro, C. M. Lee, J. M. Klymak, and A. Shcherbina, 2016: Symmetric Instability, Inertial Oscillations, and Turbulence at the Gulf Stream Front. *Journal of Physical Oceanography*, **46 (1)**, 197–217, https://doi.org/10.1175/JPO-D-15-0008.1.

Tolman, H. L., 2009: User manual and system documentation of WAVEWATCH III TM version 3.14. *Tech. rep., NOAA/ NWS/NCEP/MMAB Tech.*, 133.

Van Roekel, L. P., B. Fox-Kemper, P. P. Sullivan, P. E. Hamlington, and S. R. Haney, 2012: The form and orientation of Langmuir cells for misaligned winds and waves. *Journal of Geophysical Research: Oceans*, **117 (C5)**, 2011JC007 516, https://doi.org/10.1029/2011JC007516.

VreĆica, T., N. Pizzo, and L. Lenain, 2022: Observations of Strongly Modulated Surface Wave and Wave Breaking Statistics at a Submesoscale Front. *Journal of Physical Oceanography*, **52 (2)**, 289–304, https://doi.org/10.1175/JPO-D-21-0125.1.

Wagner, G. L., G. P. Chini, A. Ramadhan, B. Gallet, and R. Ferrari, 2021: Near-Inertial Waves and Turbulence Driven by the Growth of Swell. *Journal of Physical Oceanography*, **51 (5)**, 1337–1351, https://doi.org/10.1175/JPO-D-20-0178.1.

Wang, D., T. Kukulka, B. G. Reichl, T. Hara, I. Ginis, and P. P. Sullivan, 2018: Interaction of Langmuir Turbulence and Inertial Currents in the Ocean Surface Boundary Layer under Tropical Cyclones. *Journal of Physical Oceanography*, **48 (9)**, 1921–1940, https://doi.org/10.1175/JPO-D-17-0258.1.

Watkins, C., and D. B. Whitt, 2020: Large-Aspect-Ratio Structures in Simulated Ocean Surface Boundary Layer Turbulence under a Hurricane. *Journal of Physical Oceanography*, **50 (12)**, 3561–3584, https://doi.org/10.1175/JPO-D-20-0134.1.

Williams, R. G., A. Meijers, V. Roussenov, A. Katavouto, P. Ceppi, J. Rosser, and P. Salvi, 2024: Asymmetries in the Southern Ocean contribution to global heat and carbon uptake. *Nature Climate Change*, **14**, 823–831.

Wyngaard, J., 2010: *Turbulence in the Atmosphere*. Cambridge University Press.

Wyngaard, J., and O. Coté, 1970: The budgets of turbulent kinetic energy and temperature variance in the atmospheric surface later. *Journal of Atmospheric Sciences*, **28**.

Yu, X., A. C. Naveira Garabato, A. P. Martin, D. Gwyn Evans, and Z. Su, 2019: Wind-Forced Symmetric Instability at a Transient Mid-Ocean Front. *Geophysical Research Letters*, **46 (20)**, 11 281–11 291, https://doi.org/10.1029/2019GL084309.

Zeiden, K., J. Thomson, A. Shcherbina, and E. D'Asaro, 2024: Observations of Elevated Mixing and Periodic Structures Within Diurnal Warm Layers. *Journal of Geophysical Research: Oceans*, **129 (11)**, e2024JC021 399, https://doi.org/10.1029/2024JC021399.

Zheng, Z., R. R. Harcourt, and E. A. D'Asaro, 2021: Evaluating Monin–Obukhov Scaling in the Unstable Oceanic Surface Layer. *Journal of Physical Oceanography*, **51 (3)**, 911–930, https://doi.org/10.1175/JPO-D-20-0201.1.

Zikanov, O., D. N. Slinn, and M. R. Dhanak, 2003: Large-eddy simulations of the wind-induced turbulent Ekman layer. *Journal of Fluid Mechanics*, **495**, 343–368, https://doi.org/10.1017/S0022112003006244.

Zippel, S. F., J. T. Farrar, C. J. Zappa, and A. J. Plueddemann, 2022: Parsing the Kinetic Energy Budget of the Ocean Surface Mixed Layer. *Geophysical Research Letters*, **29**, e2021GL095 920.